TUNING OPTOELECTRONIC PROPERTIES OF III-V ALLOYS FOR OPTICAL EMITTERS VIA SPATIAL ELECTRON LOCALIZATION

TUNING OPTOELECTRONIC PROPERTIES OF III-V ALLOYS FOR OPTICAL EMITTERS VIA SPATIAL ELECTRON LOCALIZATION

CHRISTOPHER PASHARTIS, B.S.

A Thesis Submitted to the School of Graduate Studies in Partial Fulfillment of the Requirements for the Degree Master of Applied Science

MASTER OF APPLIED SCIENCE (2017) McMaster University (Materials Science and Engineering) Hamilton, Ontario

TITLE: Tuning optoelectronic properties of III-V Alloys for optical emitters via spatial electron localization

AUTHOR: Christopher Pashartis, B.S. (University of Waterloo)

SUPERVISOR: Professor Oleg Rubel

NUMBER OF PAGES: viii, 51

Abstract

The global increase in internet usage requires an upgrade of the existing infrastructure. Lasers are a key proponent to improving existing systems, and engineering better gain materials aids in this effort. (InGa)As is the leading material in this field for 1.55 μm communication wavelengths, but can be improved on by changing the substrate from InP to GaAs. Another improvement would be reducing the losses due to Auger recombination. (InGa)(BiAs) is suggested to alleviate many of these issues, as it can be grown on a GaAs substrate and is capable of decreased Auger recombination. By analyzing prospective alloys (and existing ones) using spatial electron localization, a superior candidate for industrial use can be suggested. The localization captures the disorder introduced by alloying and can be associated with material properties such as the gain characteristics and photoluminescence linewidths. These properties are important factors in determining a successor. The subject of two-dimensional materials is another topic which has shown promise in various applications. Examples include flexible, transparent, and miniaturized electronics. Recent research done by Al Balushi et al. [1] suggests that GaN may be stabilized in a two-dimensional system. By extending the material modelling approach from the telecommunication application to this system, we were able to show which III-V isoelectronic elements can be substituted into GaN. This two-dimensional system may be the only candidate capable of spanning the visible spectrum. We found Phosphorus to be the strongest candidate for decreasing the band gap.

Acknowledgments

I would like to acknowledge the constant support and source of knowledge from my supervisor Dr. Oleg Rubel. Over the time I spent with him I have gleaned many simulation techniques and analysis skills that I will forever be grateful for. The many discussions and challenges over the years have helped me develop and become a better individual.

In the two years I spent at McMaster I have met various helpful and kind people that I have had the luxury of discussions with. These include Chao Zheng, Maciej Polak, Alexandre Pofelski, Samantha Stambula, and Steffi Woo. Without their support and enlightening talks, many pieces of my research may not have come to fruition to achieve a wholesome result.

Lastly, I am indebted to my family for the amount of effort they have put into raising me and teaching me valuable life lessons. Whenever I felt troubled and required motivation, they were always there.

Table of Contents

List of Figures

List of Abbreviations

CBE	Conduction Band Edge
DFT	Density Functional Theory
DOS	Density Of States
IPR	Inverse Participation Ratio
LDOS	Localized Density of States
LED	Light Emitting Diode
LR	Localization Ratio
PL	Photoluminscence Linewidth
PR	Participation Ratio
SQS	Special Quasirandom Structure
VBE	Valence Band Edge

Chapter 1

Introduction

The main focus of the research performed was spatial electron localization, quantification of the electronic alloy disorder and its effect on optoelectronic properties. Specifically, we were interested in characterizing these properties when alloying group III-V semiconductor materials. Alloying (isovalent substitution of atoms, as opposed to non-isovalent doping) in semiconductors is important for tailoring of the band gap, lattice constant, and carrier mobility. With the exception of the lattice constants, most parameters, such as the band gaps and carrier mobilities cannot be represented as a linear combination of properties governed by the element concentrations, but rather demonstrate bowing effects. The lattice constants can be assumed to follow Vegard's Law (a linear function of the composition). Non-linearity is often argued to be due to disorder which can be seen as a perturbation to the electronic structure of an alloy. For example, consider a GaAs host semiconductor. By replacing some Ga atoms with B atoms, we are introducing significant changes in the structure which include bonding characteristics, local strain, and the addition of spatial localization of electrons.

III-V semiconductors are widely used in a variety of light emitting devices such as lasers and Light Emitting Diodes (LEDs), as well as in light absorbing devices including photodetectors and solar cells [2, 3]. The ability to engineer the band gap provides a wide set of possibilities to tailor a material to an appropriate application. For example, achieving a

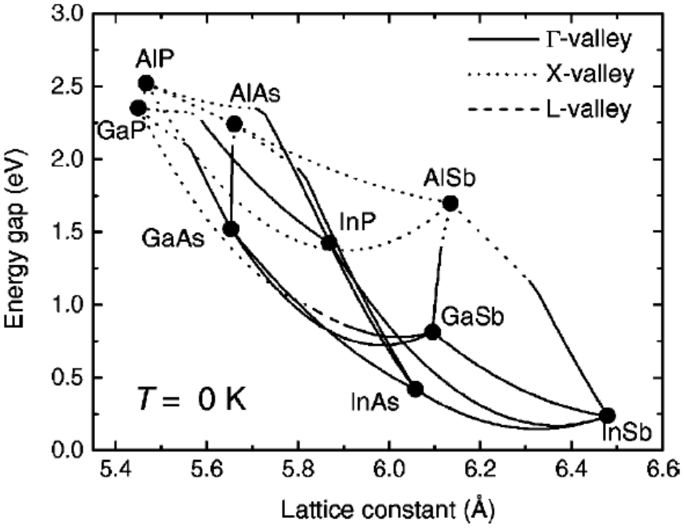

Figure 1.1: Band gaps of binary III-V semiconductors and their corresponding lattice constants. The band gaps do not vary linearly with lattice constants or composition. Reprinted from Vurgaftman et al., Journal of Applied Physics, 89, 5821, (2001), with the permission of AIP Publishing. [5]

desirable band gap while matching the lattice constant to a crystal substrate is possible (see Fig. 1.1). Predicting and tuning electronic properties of alloys is often a more difficult concept. In highly mismatched alloys, isoelectronic substitutional elements strongly affect carrier mobilities and photoluminscence linewidths. Specifically, a decrease in carrier mobilities and a broadening of the photoluminscence linewidth are observed [4]. We are able to correlate changes in some of these optoelectronic properties with spatial electron localization.

It should be noted that the papers involved in this sandwich thesis have sufficient context, therefore the thesis will serve as a supplement or medium to join these papers. We must first discuss the applications in which we can utilize electron localization to capture the changes in the properties of a material system. Most of the references and background information are provided in the papers but will be briefly summarized here.

The first subject we attempted to improve was the lasing gain medium for 1.55 μm telecommunications. Here, the so-called industry standard material is an alloy of (InGa)As. Currently, 1.55 μm lasers are not as efficient and capable as 1.3 μm devices in cooling and bit rates [6]. Previous iterations on improving the lasing medium focused on changing the substrate from InP to that of GaAs. Dilute nitrides of (InGa)(NAsSb) grown on GaAs show higher efficiencies and greater conduction band offsets, as demonstrated in 1.3 μm surface and edge lasing [7].

In the past decade, research has been carried out that suggests the current limitation to emission is due to Auger non-radiative recombination [8]. Due to the high current densities and temperatures in lasers, Auger effects are a dominant issue which affect the efficiency of emitting light. The intensity of Auger non-radiative recombination scales as the carrier density cubed ($\propto n^3$). The next generation of materials incorporated Bismuth which have been suggested to reduce the Auger effect. By incorporating Bi, the Auger rate is hypothesized to decrease when the spin-orbit split-off energy is greater than the band gap ($E_{SO} > E_{gap}$). The quaternary (BGa)(AsBi) alloy may be a new potential candidate, where the introduction of Bismuth would reduce the above mentioned Auger effect, while Boron would allow lattice matching to the GaAs substrate. In addition, we study the previous generations of alloys to compare to the new material.

In the paper, we verify the correlation between the carrier localization and a photoluminescence linewidth. The linewidth is an important property for telecommunications as a wide linewidth would introduce error over long distances - namely due to dispersion effects in optical fibres. A variance in the wavelength becomes unevenly distributed in space as a signal progresses down an optical fibre; this effect is known as pulse broadening. In addition to linewidth, changes in carrier mobility can be extracted from electron localization. Finally, lattice matching is often an important topic in lasing media as it affects the maximum possible growth thickness without dislocations. Additionally, lattice matching to a substrate introduces strain effects into the band structure. Strain has been shown to affect the polarization of light [9] as well as lifting the degeneracy of the heavy hole and light hole bands at the Γ point.

The second paper in the thesis was a study to determine the prospect of creating an emission device out of two dimensional (2D) Gallium Nitride. The growth of few-layered GaN was achieved by Al Balushi et al. [1] in 2016 (see Fig. 1.2). The structure is made stable by encapsulation with Graphene and is grown on a SiC substrate. Although this is the first experimental demonstration of 2D GaN, theoretical calculations have previously been done on 2D group III-V compounds [10, 11]. Our interest with GaN was to determine if it could span the visible light spectrum by alloying, while maintaining favourable characteristics such as high carrier mobility. 2D materials are not solely limited to emission and in recent years have gained notoriety in their potential application in transistors, photodetectors, and supercapacitors [12–14]. For example, graphene used in field effect transistors exhibit high on/off ratios [15]. Other uses are in the miniaturization of devices as well as developing flexible applications. We have done our research on monolayer hexagonal GaN as it is the most stable two-dimensional phase of the structure [11].

There are a few aspects to be aware of in regards to utilizing 2D-GaN. The band gap of monolayer GaN is indirect across the K-Γ symmetry points. This is not favourable in terms of light emission, since the recombination process requires an assistance of a phonon. In contrast, the few-layered buckled structure observed by Al Balushi et al., is not the most energetically favourable state but it has a direct band gap. There is also a remarkable

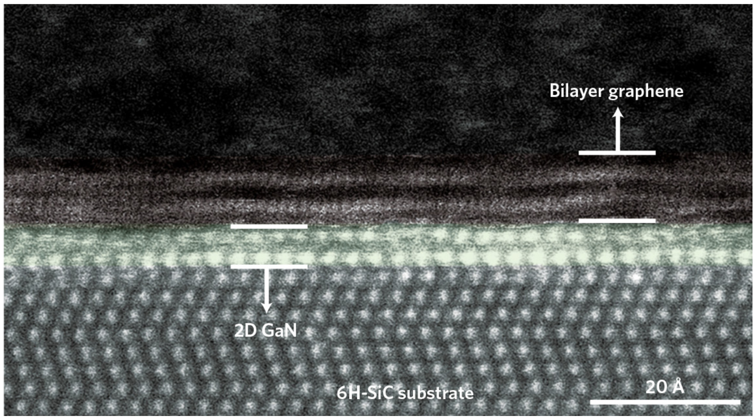

Figure 1.2: Few-layered GaN grown on a SiC substrate and encapsulated with Graphene via a migration-enhanced encapsulated growth. Graphene is used to stabilize GaN as well as aid the process via diffusion. Reprinted by permission from Macmillan Publishers Ltd: Nature Materials (Al Balushi et al., Nature Materials, 15, 1168, (2016)), copyright (2017). [1]

difference when comparing bulk wurtzite GaN to monolayer GaN; the band gap of bulk GaN is smaller and direct. This effect is due to the quantum confinement introduced in a monolayer.

A particular concern with 2D GaN is the indirect band gap. By alloying GaN with other III-V elements, we suspected and proved that in dilute concentrations a direct band gap material can be formed. Remarkably, no other two dimensional material has been found to have a band gap spanning the visible light spectrum by alloying. Existing transition metal dichalcogenides have optical band gaps in the range of 1.0-2.0 eV [16–18]. Mixing of these compounds would not extend the energy spectrum to the visible wavelengths. Various other methods for dichalcogenides have been tested, such as applying an electric field but the band gaps remain rather consistent [16]. Hexagonal BN, another two-dimensional material which is exceptionally stable at room temperature, but it has a too high optical band gap of around 5 eV [19]. The distinction between the *optical band gap* (energy of the emitted light) and the fundamental band gap in two dimensional materials is particularly important since the exciton binding energy is estimated to be around 1/4 of the band gap energy [20] and may reach values as high as several eV, while typical binding energies in bulk semiconductors are in the order of meV. This phenomenon is, however, desired in the case studied here, since monolayer GaN exhibits a band gap in the range of 4.0-5.3 eV depending on layer thickness [1, 11] and the exciton binding energy brings the optical gap and light emission to the energies of visible spectrum. To the best of our knowledge, no previous work has been done to suggest 2D GaN alloying, making this a unique study that is applicable given current techniques. Our final results aren't exact but rather suggest where these properties lie - in between a monolayer case which we studied, and the bulk wurtzite structure.

1.1 Density Functional Theory

The first-principles calculations were conducted using Density Functional Theory (DFT), which was introduced by Kohn and Sham (1965) [21]. The method solves a coupled system of partial differential equations which describes the electronic structure of a material. Specifically, we used the *WIEN2k* and *VASP* software packages in our research. In order to fully understand the methods behind DFT, it is necessary to introduce Shrödinger's equation which governs the energetics of the particles. To build this equation, let us examine the various components. For more detailed reading see [22, 23] as they form the basis of understanding below.

In the atomic scale, the Coulomb interaction governs the field of attraction and repulsion which the electrons, neutrons, and protons interact with. More precisely, we may separate a single atom into the nucleus and electrons. The energies of the particles are defined in terms of their distances from one another, d, the permittivity of free space, ϵ_0, the electron charge, e, and the atomic number, Z. The Coulomb interaction energy of an electron with another electron is,

$$E_{ee} = \frac{e^2}{4\pi\epsilon_0 d_{ee}}. \tag{1.1}$$

The energy corresponding to the Coulomb repulsion of a nucleus with another nucleus is given by,

$$E_{nn} = \frac{Z_1 Z_2 e^2}{4\pi\epsilon_0 d_{nn}}. \tag{1.2}$$

Lastly, the attraction energy between a nucleus and an electron is defined as,

$$E_{en} = -\frac{Ze^2}{4\pi\epsilon_0 d_{en}}. \tag{1.3}$$

These equations describe the electronic interactions on the simplest level.

In order to increase the accuracy of the model, we must consider that electrons are moving particles and therefore have an associated kinetic energy. The kinetic energy requires the spatial derivatives (∇) of the state of the system (a quantum mechanical effect); which is the first term in the following equation. For a single electron the Shrödinger's equation of a system depends on the position of the particle, $\vec{r}$, and the wave function, $\psi(\vec{r})$ as,

$$\left[\frac{-\hbar^2\nabla^2}{2m} + V(\vec{r})\right]\psi(\vec{r}) = E\psi(\vec{r}). \tag{1.4}$$

Where, $V(\vec{r})$ encompasses the coulomb interactions on a single electron of mass m.

In order to incorporate multiple particles into the system, we must consider the many-body wave function for N electrons at positions $\vec{r}_i$, and M nuclei at positions $\vec{R}_j$:

$$\Psi = f(\vec{r}_1, \vec{r}_2, \ldots, \vec{r}_N, \vec{R}_1, \vec{R}_2, \ldots, \vec{R}_M). \tag{1.5}$$

The wave function describes the probability amplitude of finding all of these particles at a specific positions. If all the previous effects are accounted for, then the final Hamiltonian for all the electrons and nuclei in the system resembles :

$$\Big[-\sum_i \frac{\hbar^2}{2m_i}\nabla_i^2 - \sum_I \frac{\hbar^2}{2\mathcal{M}_I}\nabla_I^2 + \frac{1}{2}\sum_{I\neq J}\frac{e^2}{4\pi\epsilon_0}\frac{Z_I Z_J}{|\vec{R}_I - \vec{R}_J|} \\ - \sum_{i,I}\frac{e^2}{4\pi\epsilon_0}\frac{Z_I}{|\vec{r}_i - \vec{R}_I|} + \frac{1}{2}\sum_{i\neq j}\frac{e^2}{4\pi\epsilon_0}\frac{1}{|\vec{r}_i - \vec{r}_j|}\Big]\Psi = E\Psi. \quad (1.6)$$

The first two terms are the kinetic energy of the electrons (i index) and nuclei (I, J indices). Where m and $\mathcal{M}$ are the masses of an electron and the nuclei at the Ith location. The next three terms describe the Coulomb interactions between two electrons, two nuclei, and a nucleus with an electron (N electrons and M nuclei). In this current form, we can appreciate the computational requirements for solving this partial differential equation which increase as the number of valence electrons and nuclei are increased; requiring further approximations.

For simplicity (but not in practice), the nuclei kinetic energy in solids tends to have a small effect on the overall energy compared to the electronic kinetic energy. Note that the uncertainty principle ensures the kinetic energy will never be zero. This reasoning is known as the Clamped Nuclei Approximation and we may remove the second term from eqn. 2.5. In a similar manner, since the nuclei have a small amount of kinetic energy we do not expect them to be displaced and may therefore consider their positions to be predetermined or a constant. We may also assume that the third term, or the nuclei-nuclei interaction, can be removed and included as part of the total energy. If we rewrite eqn. 1.6 including these three approximations, it follows that:

$$\Big[-\sum_i \frac{\nabla_i^2}{2} - \sum_{i,I}\frac{Z_I}{|\vec{r}_i - \vec{R}_I|} + \frac{1}{2}\sum_{i\neq j}\frac{1}{|\vec{r}_i - \vec{r}_j|}\Big]\Psi = E\Psi. \quad (1.7)$$

The equations become simpler to read if we use atomic units, which has been done here and for future equations in the introduction.

Decoupling the electrons and nuclei simplifies the Hamiltonian and is known as the Born-Oppenheimer approximation. The method allows us to separate the electronic interactions from the nuclei interactions. Defining the wave function as a function the positions of the electrons, $\vec{r}$,

$$\Psi(\vec{r}_1, \ldots, \vec{r}_N, \vec{R}_1, \vec{R}_2, \ldots, \vec{R_M}) \rightarrow \Psi(\vec{r}_1, \vec{r}_2, \ldots, \vec{r}_N)$$

removes the nuclei positional dependency. The Born-Oppenheimer approximation reduces the complexity of the Hamiltonian as it is now only dependent on N electrons to solve.

In its current state, the Hamiltonian is a multivariate *single* partial differential equation. If we consider each electron independent, then the electron-electron Coulomb interaction can be removed. The wave function can then be rewritten as a product of independent wave functions for each electron, $\psi_i(\vec{r}_i)$, as

$$\Psi(\vec{r}_1, \ldots, \vec{r}_N) = \prod_i^N \psi_i(\vec{r}_i). \tag{1.8}$$

This approximation is known as the Hartree product; allowing the Hamiltonian in eqn. 1.7 to be split into N individual equations. The process removes the electron-electron interaction, which is an important physical component of the Hamiltonian. It will be accounted for later. For now, this is a good assumption and we can begin to include a few quantum mechanical effects.

Since electrons are considered anti-symmetric (they are fermionic) the wave functions must correctly model this behaviour. Overlooking the details, if a wave function is symmetric then the particle positions may be swapped without a change in the wave function, and vice versa for an anti-symmetric wave function. Namely, in an anti-symmetric wave function of two particles,

$$\Psi(\vec{r}_1, \vec{r}_2) = -\Psi(\vec{r}_2, \vec{r}_1). \tag{1.9}$$

To incorporate this feature for a two particle system, the wave function as a product of individual wave functions, would take the form of

$$\Psi(\vec{r}_1, \vec{r}_2) = \frac{1}{\sqrt{2}} \left[\psi_1(\vec{r}_1)\psi_2(\vec{r}_2) - \psi_1(\vec{r}_2)\psi_2(\vec{r}_1)\right]. \tag{1.10}$$

In order to apply the anti-symmetric properties to the many-electron case consider the Slater determinant,

$$\Psi(\vec{r}_1, \ldots, \vec{r}_N) = \frac{1}{\sqrt{N!}} \begin{vmatrix} \psi_1(\vec{r}_1) & \cdots & \psi_N(\vec{r}_1) \\ \vdots & \ddots & \vdots \\ \psi_1(\vec{r}_N) & \cdots & \psi_N(\vec{r}_N) \end{vmatrix}. \tag{1.11}$$

In this manner, the Pauli exclusion principle is satisfied.

The last piece that we require to fully capture our electronic structure in the model is the reintroduction of the electron-electron interaction. Recall, the interaction was removed earlier to introduce the Hartree product. To re-include the electron-electron physics an electron density is introduced, inspired by Poisson's equation:

$$\nabla^2\phi(\vec{r}) = 4\pi n(\vec{r}). \tag{1.12}$$

Where $\phi(\vec{r})$ is the electrostatic potential and $n(\vec{r})$ is the charge density. The Coulomb interaction is incorporated as the Hartree Potential, $V_H = -\phi(\vec{r})$, or in atomic units:

$$V_H = \int \frac{n(\vec{r}')}{|\vec{r} - \vec{r}'|} d\vec{r}'. \tag{1.13}$$

The Hartree Potential does include a self-interaction component. If we consider the probability of finding an electron as an electron density, then the electron charge density can be represented by a probability density as

$$n(\vec{r}) = \sum_i \psi_i(\vec{r})^* \psi_i(\vec{r}). \tag{1.14}$$

However, there is still a lack of an 'exchange' between the electrons after removing it earlier. We introduce the exchange potential, V_X, to include the energies involved with Pauli's exclusion principle. In addition, we require an energy that entails the correlation of an electron with another electron. Quantum mechanically, no electron is independent of another electron, there is an inherent correlation between any two electrons. This correlation interaction energy is defined as V_C. In the simpler Hatree-Fock Hamiltonian, exchange is included but not the correlation. The Kohn-Sham formulation [21] of a single electron interaction in a system is then given (simply) as

$$H\psi_i(\vec{r}) = \left[-\frac{1}{2}\nabla^2 + V_n(\vec{r}) + V_H(\vec{r}) + V_X(\vec{r}) + V_C(\vec{r}) \right] \psi_i(\vec{r}). \tag{1.15}$$

One may wonder why this formulation is defined as *Density Functional Theory*. It is derived from the interaction terms of the Hamiltonian. The Hartree potential is a function of the electron density which itself is a function of the electron position. In other words, the Hartree Potential function is dependent on a function - it is a functional. The method to solve this Kohn-Sham Hamiltonian is dependent on the Hohenberg-Kohn theorems. The theorems help to define the translation between the Many-Body formalism to the electron density formalism. Perhaps the most important point of this theorem (and in others too) is that the lowest energy for a system corresponds to the ground state energy. The remaining difficulty with our up to date model, is how to define the Exchange and Correlation potentials, typically written together as V_{XC}. Presently, the academic community has no exact solution to these functionals. As a result, there have been many approximations over the years.

The first estimation was known as the Local Density Approximation (LDA) which was introduced alongside the Kohn-Sham equations [21] and numerically popularized by Ceperley and Alder, and Perdew and Wang [24, 25]. Its nomenclature derives from the dependency of the Exchange-Correlation Potential on the electron density at the same point. The LDA is often perceived as analogous to a homogeneous electron gas approach, or as some prefer to call it - a homogeneous electron gas in a box. The second most known approximation is the so-called Generalized Gradient Approximation (GGA) found by Becke [26] with the most common numerical implementation by Perdew et al. [27], which involved the Exchange Correlation Potential as a function of the gradient of the electron density.

In the LDA and GGA formalism, there are many subgroups of the functionals which approximate the general concept. The various subgroups are excellent at predicting parameters of materials to different accuracies. Examples include lattice constants, band gaps, band offsets, optical properties, and magnetism. It is important to note that while LDA and GGA are both sufficient, they can yield drastically different results. Perhaps one of the more well known differences is their abilities to predict spontaneous magnetism in Iron, where GGA will predict ferromagnetism but LDA will not. Additional approximations to the functional do exist in the form of Hybrid Functionals or Meta-GGA that correct the band gaps of a material but are often more computationally intensive. At this point it would seem to the novice reader in DFT that the specific use of a functional is dependent on the property in which one wishes to simulate. The fact that the correct functional has to be chosen may be somewhat of a conundrum given that it is a first-principles based calculation. This is particularly why many studies have been done correlating many theoretical properties to that of the experimental values.

Chapter 2

Disorder in Alloys

The alloying process is an effective method to tune the properties of an existing III-V material. However, there are many characteristics to observe as the composition of the material changes. The properties we are interested in are Photoluminescence Linewidths (PL), optical gain, carrier mobility, and band gap energies. When comparing multiple materials, it can be quite difficult to account for all these properties to determine the most suitable alloy. To properly distinguish the strongest candidate for an application, one can study the electronic disorder introduced by alloying. Using the electron localization as a measure of disorder we may quantify the changes introduced into the PL, gain properties, and carrier mobility. These properties are important in determining the suitability of application of a material in devices such as solar cells, lasing media, and LEDs. An example of a change in electron effective mass due to disorder is demonstrated in Fig. 2.1, while a broadening of light hole transition states may be seen in Fig. 2.2.

Disorder can be described using spatial electron localization; a quantity readily available from simulations. An example of disorder induced change in a material property may be as follows: an increase in localization would signify a decrease in carrier mobility at the band edges. This relationship would imply a reduction in solar cell capability to evacuate excitons before they recombine.

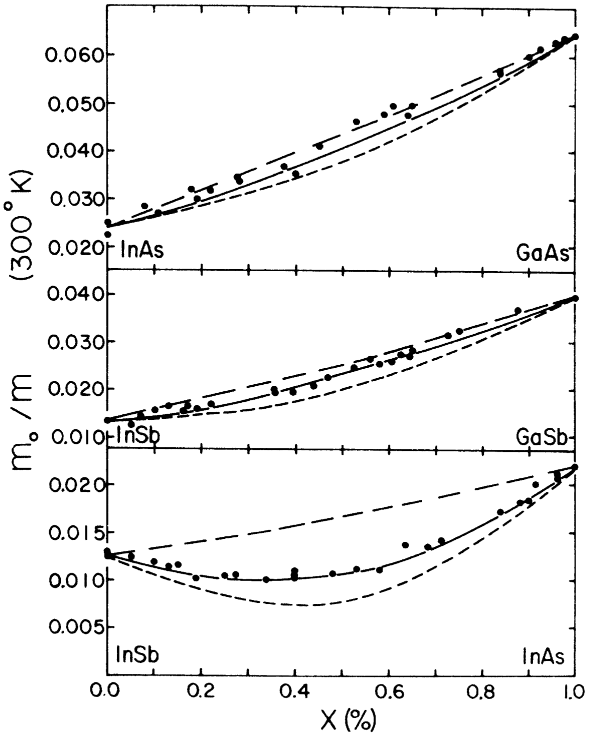

Figure 2.1: Changes in composition introduces disorder into the host structure forcing non-linear change in the electron effective mass values at the Γ-point [28]. Reprinted (Fig.1) with permission from Berolo et al., Physical Review B, 8, 3795, (1973). Copyright 2017 by the American Physical Society. [28]

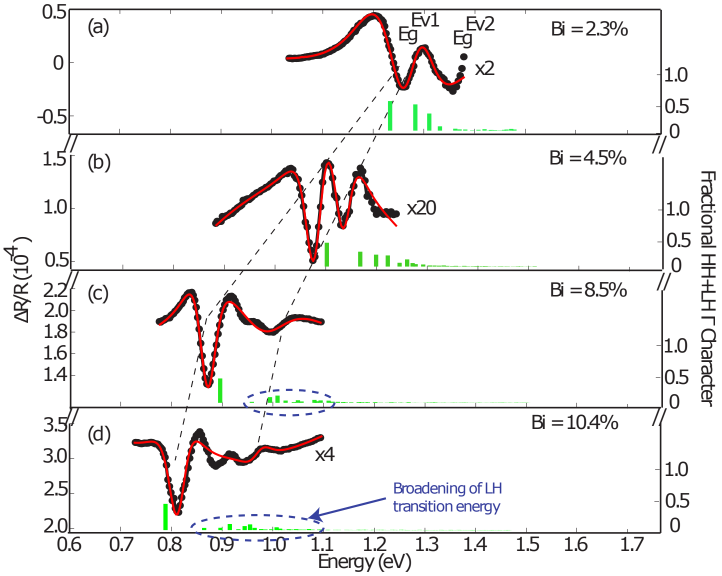

Figure 2.2: Increasing the composition of Bi in a GaAsBi alloy shows a broadening of the Light Hole (LH) energy states, implying a broadening of the PL spectrum. Reprinted (Fig.1) with permission from Usman et al., Physical Review B, 8, 3795, (2013). Copyright 2017 by the American Physical Society. [4]

2.1 Spatial Electron Localization

We begin with the description of finding an electron at an eigenenergy, E, in a given volume of space (see Fig. 2.3) as

$$\rho = \int_0^r \Psi(r)\Psi^*(r)dr^3. \tag{2.1}$$

Where $\Psi_i(r)$ are the normalized wave functions. In any material there exists an array of sites in which electrons will most likely be situated. To capture the proposed physical properties mentioned previously, we are interested in the regions around N atomic sites denoted by the index i. The total probability of finding an electron at an eigenenergy around atomic sites

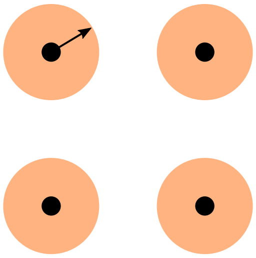

Figure 2.3: A simple example of 4 atoms where we define the orange (shaded) area around the atoms as the region enclosed by $\vec{r}$. In an alloyed case the radii would be different among different atoms to capture the appropriate electronic states.

of predefined radii would be

$$r_{tot} = \sum_{i}^{N} \int_{0}^{r_i} \Psi(r)\Psi^*(r)dr^3 \tag{2.2}$$

With respect to the radii, the values are often standardized, such as in *VASP*. In *WIEN2k*, these regions are arbitrary and are dependent on the muffin tin spheres selected to include the core wave functions.

2.2 Localization Ratio

The most fundamental approach to quantifying localization would be to consider the probabilities of finding a carrier around an atom. This is a direct relationship to the equations shown earlier. For example, if the host material is GaAs and an In atom is substituted for a Ga atom, then the resultant electron localization will be shifted from the host substituted site. To capture this effect consider the change in probability at the substituted site as

$$\zeta = \frac{\rho_{\mathrm{In}}}{\rho_{\mathrm{avg:Ga}}} - 1. \tag{2.3}$$

This is essentially a percent difference of the amount of the probability from the expected or original value. This method was initially introduced by Deng et al. [29] known as the

Localization Ratio (LR) which demonstrates the shift in the density of the substituted site. It has the following values:

$$\zeta = \begin{cases} < 0 & \text{localization loss} \\ 0 & \text{no change in localization} \\ > 0 & \text{localization increase.} \end{cases}$$

LR captures a shift around a *single* atomic site, which is not useful when discussing the entire material and the effects of localization on electronic or optical properties. Once disorder is introduced into a system it affects the structure, not a specific site. Therefore, LR is unrepresentative as to how the mobility of carriers or the PL will change for an alloy.

2.3 Localization by Data Mining

Given a large amount of data, the possibility to distinguish a localized carrier relative to a delocalized structure at a given energy was examined. Although this method was indeed replaced with the more rigorous generalized Participation Ratio (PR) later on, it is nonetheless an important aspect of this thesis which will be briefly summarized. The basis of this method was inspired by the following question: given a set of probabilities how does one determine if a carrier is centred on specific atoms? There are a few methods which were considered to approach this problem. One could train a neural algorithm, local density estimation (for multivariate systems), or one could try to select localized data by defining it as an outlier via a quartile method. For a detailed description of many methods see Welsh (2011) [30].

The quartile method [31] (commonly known as a boxplot) utilizes the following scheme to determine if a value, x, is considered part of the data set:

$$Q_1 - \mu \cdot IQR \leq x \leq Q_3 + \mu \cdot IQR. \tag{2.4}$$

Where μ is known as the whisker range, or how extreme one is willing to consider data to be part of the baseline. For reference, the standard value for μ is 1.5 which corresponds to the standard deviation of a Gaussian distribution. IQR is the interquartile range; the difference between Q_1 and Q_3. The deviation was tuned such that the standard material, which is expected to be disorder free, would show no outliers. Additionally, Q_1 and Q_3, are the first and third quartiles of the data set - the 25th and 75th percentile. By using this process we can accurately observe the localization (or lack of) in a few benchmark scenarios:

- *Uniform Distribution of Data* - Carrier probabilities can be equally spread out across a dataset, as is the case in binary materials such as GaAs. Here, the carrier probabilities around Ga atoms are equivalent; likewise with As atoms.
- *Localization at a Single Atom* - Should there be a single peak or extremum, the quartile method must be able to detect the localization, which by construction it will.
- *Localization on a Group* - There is often a discrepancy between the sublattices due to the differing charge densities found on the groups. To account for the differences,the probabilities must be partitioned to compare with its respective sublattice. An example of this process can be seen in Fig. 2.4.

The quartile method comes with a caveat; it picks specifically which atoms demonstrate spatial localization *with respect to the other atoms*. This corresponds to capturing a portion

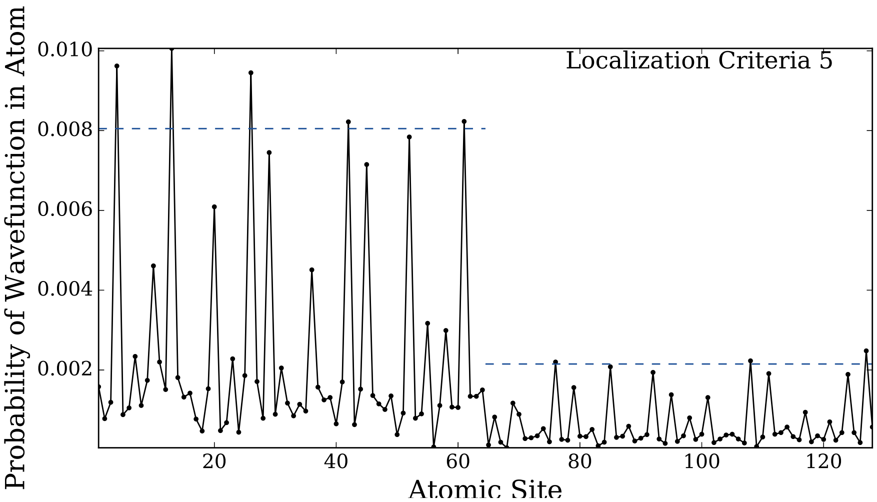

Figure 2.4: An example of the quartile method being split between group III/V sublattices, left and right respectively. The dotted blue line indicates the cutoff considered for the baseline; any value above is determined to be a localized state. A localization criteria of 5 was used, corresponding to the value of μ.

of the Density of States (DOS) of the material and therefore must be scaled appropriately to reflect the material volume. The scaling is important when comparing various alloys derived from the same host structure. For example, if the host structure is GaAs and one wishes to consider the localization between $\mathrm{In}_y\mathrm{Ga}_{1-y}\mathrm{As}$ and $\mathrm{GaAs}_{1-x}\mathrm{N}_x$.

In summary, the quartile method is effective at selecting outliers - which is equivalent to localization. The drawback to the procedure is that it selects individual atoms with no theoretical relationship to optoelectronic properties. As a tool for studying localization data, the quartile method may be useful, but it cannot imply any changes in the properties of a material with certainty.

2.4 Generalized Participation Ratio

The disadvantage of both of the previous methods is their lack of relationship to optoelectronic properties. The solution to this problem was introduced by Wegner (1980) [32], where he analyzed the second moment of the probability known as the Inverse Participation Ratio (IPR)

$$\chi(E_i) = \frac{\int |\psi(\mathbf{r})|^4 d\mathbf{r}}{\left[\int |\psi(\mathbf{r})|^2 d\mathbf{r}\right]^2}. \tag{2.5}$$

This method is related to the normalized variance of a sample set; it captures the variance in finding a carrier at an eigenenergy E_i, at any atomic site. Once again, there are a few regimes which are important in understanding this quantitative measure:

$$\chi = \begin{cases} 1/N & \text{equal localization across all sites in the lattice, i.e. no localization} \\ 1 & \text{complete localization of the wave function on a single atomic site} \end{cases}$$

Note that in the Thermodynamic limit ($N \to \infty$), the IPR goes to 0 as expected.

A significant amount of research has been conducted since the introduction of IPR, demonstrating its capability as a quantity. First is its relation to the Anderson localization [33] or the absence of diffusion. In this case, the movement of carriers is characterized by site hopping due to very localized states. The lack of DC conductivity at zero temperature occurs due to localized states near the Fermi energy. In relation to the Anderson model, a localization length is often discussed where there is a sharp transition that defines this vanishing behaviour. The relationship between Anderson Localization and the IPR is documented theoretically by Kramer and MacKinnon [34]. A more recent example of the IPR being directly related to the conductive properties of a material was observed by Schwartz et al. [35]. They showed that at the Anderson transition the large fluctuations in the IPR confirm its relationship with conductivity.

Chapter 3

Properties of Materials

This section outlines the details of a few properties of materials and methodologies required to understand the research conducted.

3.1 Band Unfolding

The band structures of materials within the range of plus or minus the band gap of a material ($\pm E_{gap}$) were studied in the research. This region pertains to the energies required in Auger recombination. In addition, a study of the band edges enables a discussion of carrier mobilities and broadening of PLs. Unfortunately, due to the nature of alloy calculations, a distinct bandstructure is difficult to obtain. The ambiguity is due to the Brillouin zone of the primitive cell folding onto itself in supercell calculations. In tightbinding models and k·p models, the inherent disorder cannot be found since exact band dispersion is assumed (see tightbinding examples Fig. 3.1). The research herein uses the method of Bloch spectral functions which was numerically implemented in *VASP* and *WIEN2k* by Rubel et al. [36] to recover the primitive brillouin zone picture of the disordered alloy's band structure. It is summarized here in the same formalism.

The method considers the plane wave expansion of a wave function at a given eigenenergy,

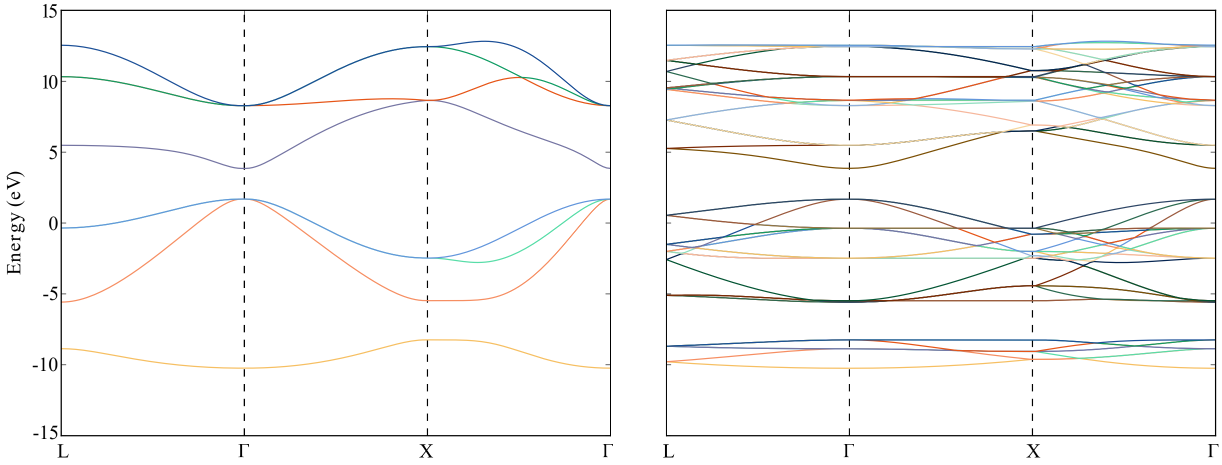

Figure 3.1: Folding of the bandstructure going from a 2-atom primitive cell (left) to an 8-atom supercell (right) with the tightbinding model. The concept of reverting the 8-atom supercell to a 2-atom primitive cell is the essence of the unfolding technique. The disorder introduced by alloying prevents unfolding with certainty in DFT.

ϵ_n:

$$\Psi_{n,\vec{K}(\vec{r})} = \sum_{\vec{G}} C_{n,\vec{K}}(\vec{G}) e^{i(\vec{K}+\vec{G})\cdot\vec{r}}. \tag{3.1}$$

Where $C_{n,\vec{K}}$ is an expansion coefficient, $\vec{K}$ is the reciprocal lattice vector and $\vec{G}$ is the reciprocal lattice vector shift to a neighbouring Brillouin Zone. The primitive reciprocal lattice vector, $\vec{k}$, is equivalent to a transformation of the supercell vectors by

$$\vec{k} = \vec{K} + m_1\vec{G}_1 + m_2\vec{G}_2 + m_3\vec{G}_3. \tag{3.2}$$

Where $m \in 0 \ldots N-1$ and N is the number of expansions to create the supercell from the primitive structure. In this process, the wave functions are rewritten in the primitive cell basis.

The *spectral weight* describes the Bloch character of an eigenenergy as,

$$w_n(\vec{k}) = \sum_{\vec{g}} |C_{n,\vec{K}}(\vec{k} + \vec{g})|^2. \tag{3.3}$$

Here, $\vec{g}$, is the shift to a neighbouring Brillouin Zone in the primitive cell basis. This Bloch character or spectral weight must sum to 1 for a given eigenenergy,

$$\sum_{\vec{k}} w_n(\vec{k}) = 1. \tag{3.4}$$

In a primitive structure, the Bloch character is defined as the Kronecker delta about the radius of an atomic sphere. In a supercell structure, the peak widens and the Bloch character is spread out over the reciprocal space. Note that the Bloch character for a specific value decreases with increased spatial localization. In other words, a large Bloch character is correlated with no spatial localization and vice versa.

3.2 Born Effective Charge

In an isolated environment or vacuum around an element, a common method to understand how strongly an atom may be attracting electrons is reflected by electronegativity. In a material, the definition of electronegativity no longer retains its description. The Born effective charge is an alternative measure in which to quantify the electronegativity in a material structure. By studying the change in the Born effective charge, changes in bonding characteristics or valence/conduction band edge shifts can be explained. Various techniques are used to evaluate these charges in DFT. The methods may make use of Berry Phases, density functional perturbation theory, or finite electric field adjustments.

3.3 Special Quasirandom Structures for Alloying

In order to achieve a structure as close to a perfectly random as possible, we must include the pair correlations between like-atoms. Zunger et al. (1990) [37] introduced the notion of Special Quasirandom Structures (SQS) as a method to include the correlations between atoms when randomizing a structure. It was incorporated by van de Walle et al. (2013) [38] with the *Automated Alloy Theoretic Toolkit*, which uses a Metropolis Monte Carlo algorithm to find the most favourable SQS. Specifically, the code minimizes the following function,

$$Q = \frac{1}{4}\omega L + \sum_{\alpha \in A} |\Delta \rho_\alpha(\sigma)|. \tag{3.5}$$

The value of Q is the objective function in which the algorithm attempts to minimize. Here, ω is a user-defined weight and L is the maximum pair length. The sum is over all *clusters*, A, of the changes in correlation ($\Delta \rho_\alpha$) from a purely random state at a given atomic occupation σ, to that of the current distribution. The *clusters* refer to the various geometries used to define the types of correlations that exist. There are pair correlations (2 atoms), triplet correlations (3 atoms), and quadruplet correlations (4 atoms). Based on a user defined distance for each correlation, the code determines the best minimized state. An example of the minimization time line of the correlation changes can be found in Fig. 3.2.

This minimization algorithm process is as follows:

- Generate a random starting point for a supercell given the alloy composition
- Begin an annealing loop (where the user can define an annealing temperature, T) to sample the space for the optimal solution, using $exp(-Q/T)$ to permute two atoms. This is similar to an Ising Model algorithm

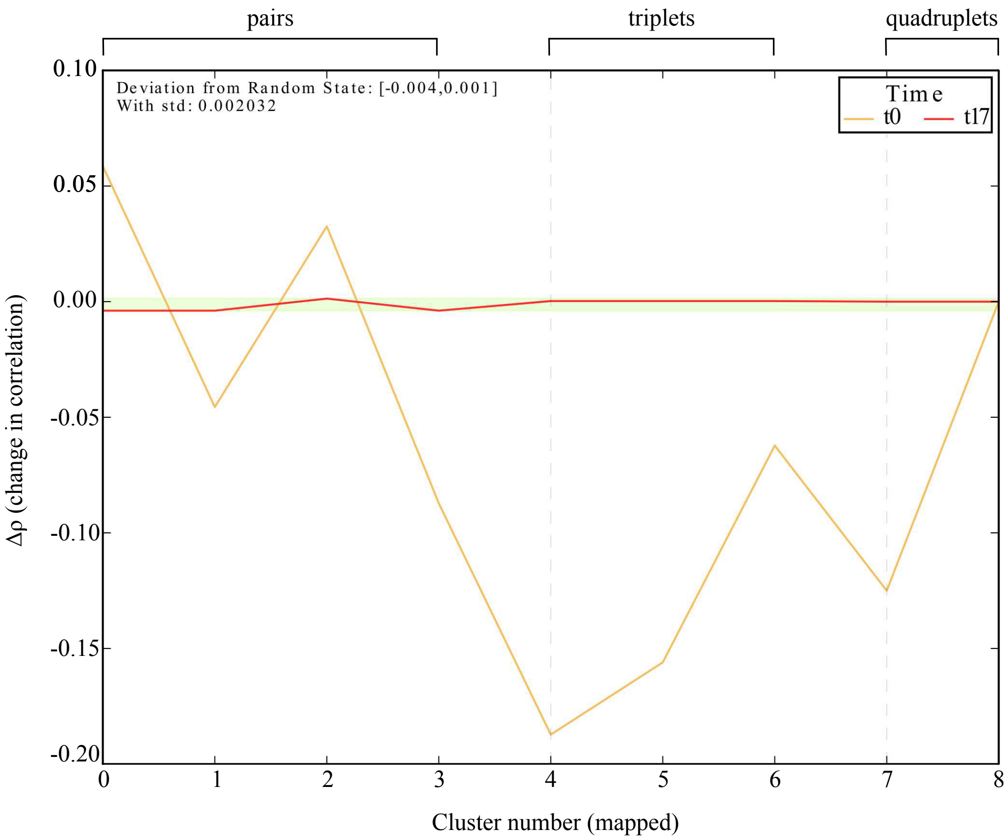

Figure 3.2: An, example of the SQS convergence of the cluster correlations. The ideal situation would be that $\Delta\rho$ approaches zero. The orange line is the starting position and the final position is the red line. The dotted vertical lines distinguish between pair, triplet, and quadruplet correlations respectively.

- The result is compared to the best-case scenario and determined if further minimization is required

Chapter 4

Localization of Electronic States in III-V Semiconductor Alloys: A Comparative Study

Reprinted article with permission from C. Pashartis and O. Rubel, Physical Review Applied, 7, 064011, 2017. Copyright 2017 by the American Physical Society. https://doi.org/10.1103/PhysRevApplied.7.064011

4.1 Author's Contribution

- Analyzing and generating SQS
- Developing localization criteria
- Born effective charge calculations
- Literature evaluation
- Preparation of manuscript draft

PHYSICAL REVIEW APPLIED **7,** 064011 (2017)

Localization of Electronic States in III-V Semiconductor Alloys: A Comparative Study

C. Pashartis and O. Rubel[*]

Department of Materials Science and Engineering, McMaster University,
1280 Main Street West, Hamilton, Ontario L8S 4L8, Canada

(Received 24 December 2016; revised manuscript received 3 May 2017; published 12 June 2017)

Electronic properties of III-V semiconductor alloys are examined using first principles, with the focus on the spatial localization of electronic states. We compare localization at the band edges due to various isovalent impurities in a host GaAs, including its impact on the photoluminescence linewidths and carrier mobilities. The extremity of localization at the band edges is correlated with the ability of individual elements to change the band gap and the relative band alignment. Additionally, the formation energies of substitutional defects are calculated and linked to challenges associated with the growth and formability of alloys. A spectrally resolved inverse participation ratio is used to map localization in prospective GaAs-based materials alloyed with B, N, In, Sb, and Bi for 1.55-μm-wavelength telecommunication lasers. This analysis is complemented by a band unfolding of the electronic structure and a discussion of the implications of localization on the optical gain and Auger losses. Correspondence with experimental data on the broadening of the photoluminescence spectrum and charge-carrier mobilities show that the localization characteristics can serve as a guideline for the engineering of semiconductor alloys.

DOI: 10.1103/PhysRevApplied.7.064011

I. INTRODUCTION

Semiconductor alloys are widely used as an active material in a variety of optoelectronic applications, such as lasers, solar cells, light-emitting diodes (LEDs), and photodetectors [1]. For instance, dilute bismides Ga(As,Bi) [2,3], dilute nitrides (Ga,In)(N,As) [4,5], and group-III nitrides (Al,Ga,In)N [6] represent group-III-V materials that are actively studied. Mixing of semiconductors enables tuning of their optical properties, lattice parameters (epitaxial strain), and transport characteristics to a desired application. Examples include 1.55-μm emission wavelength in the telecommunications industry, the visible spectrum for general lighting, an ultraviolet range of wavelengths for disinfecting water, and a multijunction monolithic solar cell with 1-eV absorption edge.

Properties of the solid solutions often deviate from Vegard's law; i.e., they cannot be represented as a linear interpolation between properties of the constituents. Alloying elements perturb the electronic structure of the host material, which may introduce traps that affect the optical and transport characteristics. For instance, a band-gap bowing [7] and a broadening of the photoluminescence (PL) linewidth in dilute nitride semiconductors [8], or a drastic decrease of the hole mobility in dilute bismides [9], are attributed to band tails, which originate from the spatially localized states created by isoelectronic substitutional impurities of individual N or Bi as well as their clusters in a GaAs host [10–13]. Extrinsic factors, such as nonintentional dopant impurities, native defects, and heterostructure interfaces, also contribute to localization; however, we will examine intrinsic factors only in our study.

Localization of electronic states can detrimentally affect the performance of devices, which should be taken into account when selecting alloying elements. In the case of solar cells, high mobility is desired for the efficient transport of photogenerated carriers to electrodes. The presence of band tails leads to an inhomogeneous broadening of the gain spectrum, causing a reduction of the peak value of intensity gain (Ref. [14], p. 221). On the other hand, a wide photoluminescence linewidth can be a desired attribute in the case of ultraviolet light sources for water purification [6] or a general-purpose LED lighting [15].

Electronic-structure calculations are widely used to explore parameter space [16] and aid in quantifying the disorder introduced into a system by isoelectronic substitutional impurities. For example, GaP:N, GaAs:Bi, and GaN:As exhibit strong spatial localization of wave functions associated with impurity states near the band edges [10, 17–20]. Examination of a three-dimensional charge-density distribution associated with an electronic state in an alloy provides some information about the extent of localization, but it lacks a quantitative criterion that distinguishes between localized and delocalized states.

Bellaiche *et al.* [17] originally proposed a localization parameter as a sum of probabilities $\rho_\alpha(E_i)$ for finding an electron in a specific eigenstate E_i in the vicinity of atomic sites α of the same element type. Deng *et al.* [21] adapted this approach to a single impurity, e.g., GaAs:X, and defined a localization ratio as the ratio of the wave-function probability amplitude at the impurity site X relative to the element it is substituted for in the host lattice,

---

[*] rubelo@mcmaster.ca

$$\zeta = \frac{\rho_X}{\rho_{\mathrm{Ga\,or\,As}}} - 1. \tag{1}$$

The stronger the localization is, the higher the ratio; the ratio of zero corresponds to no spatial perturbations of the electronic state. The magnitude of the ratio can be used to assess the relative impact of various impurities on the band edges of the host. However, a generalization of this approach to an *arbitrary* state in an alloy is not straightforward due to the lack of a "reference" state.

Localization in alloys can be defined as a vanishing zero-temperature dc conductivity in the system (the absence of diffusion in the Anderson model [22]). The value of conductivity as a function of the Fermi energy provides a spectral measure of localization. However, its calculation from first principles is a cumbersome process. Instead, Wegner [23] suggested the second moment of the wave-function probability amplitude, i.e., the inverse participation ratio (IPR)

$$\chi(E_i) = \frac{\int |\psi_i(\boldsymbol{r})|^4 d\boldsymbol{r}}{[\int |\psi_i(\boldsymbol{r})|^2 d\boldsymbol{r}]^2}, \tag{2}$$

as a criterion to distinguish between localized and extended states. The inverse value χ^{-1} represents a volume within which the wave function $\psi_i(\boldsymbol{r})$ is confined. It can also be related to the probability of an electron to return to the same state after an infinite time interval [24] and thus is ultimately linked to the transport properties.

Here, we use both the localization ratio and the IPR criteria to perform a comparative study of localization effects in group-III-V semiconductor alloys. First, we characterize isovalent impurities of B, N, Al, P, In, Sb, Tl, and Bi in the host GaAs. We show that the localization strength of these impurities is governed by their Born effective charges. The strength of localization also determines the ability of alloying elements to change the band gap and the relative alignment of the conduction- and valence-band edges (the CBEs and VBEs), which is important for band-gap engineering. Additionally, formation enthalpies of the individual impurities are calculated and linked to challenges associated with the growth of corresponding alloys. Finally, we compare disorder characteristics of various gain-medium materials for 1.55-μm lasers, including $\mathrm{Ga}_{1-x}\mathrm{In}_x\mathrm{As}$, dilute $\mathrm{Ga}_{1-x}\mathrm{In}_x\mathrm{As}_{1-y-z}\mathrm{N}_y\mathrm{Sb}_z$, and $\mathrm{GaAs}_{1-x}\mathrm{Bi}_x$ alloys, as well as the hypothetical $\mathrm{Ga}_{1-x}\mathrm{B}_x\mathrm{As}_{1-y}\mathrm{Bi}_y$ compound alloys. The results of the aforementioned calculations are related to established experimental trends in transport coefficients and the PL characteristics of these alloys.

II. COMPUTATIONAL DETAILS

A. Electronic structure of binaries, impurities, and alloys

The first-principles calculations are carried out using density-functional theory (DFT) [25] and the linear augmented plane-wave method implemented in the WIEN2K package, version 14.2 [26]. The Brillouin zone of the binary compounds' primitive cell is sampled using $8 \times 8 \times 8$ Monkhorst and Pack [27] mesh. The muffin-tin radii R^{MT} were set to 1.72, 1.85, 1.90, 1.95, 2.00, 2.00, 2.10, 2.31, 2.33, and 2.33 bohr for N, B, P, Al, Ga, As, In, Sb, Tl, and Bi, respectively. The product $R^{\mathrm{MT}}_{\mathrm{min}} K_{\mathrm{max}} = 7$, which determines the accuracy of a plane-wave expansion of the wave function, is used throughout the calculations.

TABLE I. Equilibrium lattice constant a_0, band gap E_g of binary compounds in the zinc-blende structure calculated with the DFT-GGA-WC-MBJ method and compared with the experimental values gathered in Refs. [30,31].

	DFT		Experiment	
Binary compounds	a_0 (Å)	E_g (eV)	a_0 (Å)	E_g (eV)
BAs	4.775	1.66	⋯	⋯
BBi	5.471	0.39	⋯	⋯
GaN	4.507	2.96	4.50	3.30
GaAs	5.660	1.53	5.609	1.52
GaSb	6.116	0.72	6.096	0.81
GaBi	6.368	−1.65	⋯	⋯
InN	4.995	0.66	4.98	0.78
InAs	6.091	0.52	6.058	0.42
InSb	6.526	0.17	6.479	0.24

The lattice constants and the band structures of the binary compounds (Table I) are calculated self-consistently using the Wu and Cohen [28] generalized-gradient approximation (GGA WC) for the exchange-correlation functional. The choice of exchange-correlation functional is based on preliminary studies of the band structure of GaAs [20]. The Tran-Blaha modified Becke-Johnson (TBMBJ) potential [29] is applied to overcome deficiency of the semilocal exchange-correlation functional and to improve the accuracy of the band gaps.

We build 128-atom $4 \times 4 \times 4$ supercells using a two-atom primitive-cell basis instead of the conventional eight-atom cell required for calculation of the effective band structure of an alloy. The k mesh is downscaled to $2 \times 2 \times 2$. The GGA-WC self-consistent lattice constant of $a_0 = 5.660$ Å is used for the host GaAs in the single-impurity studies. The list of alloys, their bond compositions, and the expectation values of the lattice parameters are provided in Table II. In the case of alloys, the lattice constant is obtained from a linear interpolation by taking into consideration the equivalent binary concentration of the bonds. The atomic positions are optimized by minimizing Hellmann-Feynman forces acting on atoms below 2 mRy/bohr. Calculations of the Bloch spectral weight for the effective band structure are performed using the FOLD2BLOCH package [32]. Born effective charges for impurities are computed using a BERRYPI module [33] implemented in WIEN2K.

A localization ratio ζ defined in Eq. (1) is used to evaluate the extent of localization at the band edges for

TABLE II. The bond statistics used to determine the lattice constant of alloys based on Vegard's law. These concentrations are determined by the number of bonds in the supercell. Deviations from a random alloy such as enhancement of a particular bond statistics due to short-range correlations are marked in parentheses. The sum of the concentrations adds up to 1.

	Equivalent binary concentration c_i									$a = \sum_i c_i a_0(i)$
Supercell composition	BAs	BBi	GaN	GaAs	GaSb	GaBi	InN	InAs	InSb	(Å)
$In_{34}Ga_{30}As_{64}$				0.469				0.531		5.89
$Ga_{38}In_{26}As_{60}N_2Sb_2$ (In-N correlated)				0.574	0.020		0.031	0.363	0.012	5.81
$Ga_{64}As_{57}Bi_7$				0.891		0.109				5.74
$Ga_{58}B_6As_{57}Bi_7$ (B-Bi correlated)	0.057	0.036		0.832		0.075				5.65

single impurities. An arithmetic averaging of ζ's is performed to account for degeneracies at the band edges. We find the results to be sensitive to the size of the supercell. For instance, Deng *et al.* [21] report $\zeta = 3.5$ at the valence-band edge for a 64-atom GaAs:Bi supercell, which can be compared to our result of $\zeta = 5.1$ for a 128-atom supercell but differs from the value of $\zeta = 16$, which is obtained under identical conditions for a 432-atom supercell. Here, we constrain the size of a supercell to 128 atoms, which implies that the localization ratio may not be fully converged with respect to cell size. Nevertheless, chemical trends in a relative localization ratio ζ computed for various impurities should be valid.

The IPR χ is used as a measure of localization in alloys. It is evaluated on the basis of probabilities of finding an electron with an eigenenergy E_i within the muffin-tin spheres centered at atomic sites. The atomic sites, α, and, correspondingly, the IPR values are split into two sublattices: groups III and V. The IPR is evaluated for each sublattice using a discrete version [34] of Eq. (2),

$$\chi^{\mathrm{III/V}}(E_i) = \frac{\sum_\alpha \rho_\alpha^2(E_i)}{[\sum_\alpha \rho_\alpha(E_i)]^2}. \tag{3}$$

The summation index α runs over all atomic sites on the group-III or -V sublattice. Here, the participation ratio χ^{-1} represents a number of atomic sites which confine the wave function $\psi_i(\boldsymbol{r})$. The lower limit of the IPR is the inverse number of atoms in the sublattice that corresponds to the pure Bloch states. The spectrally resolved IPR is determined as a weighted average

$$\chi(E_i) = \frac{\chi^{\mathrm{III}} w^{\mathrm{III}} + \chi^V w^V}{w^{\mathrm{III}} + w^V}, \tag{4}$$

where $w = \sum_\alpha \rho_\alpha(E_i)$ is the eigenstate-specific weight calculated for each group of atoms. It should be noted that the muffin-tin spheres capture only a portion of the wave function (50% or less in typical calculations reported here). The remaining part of the wave function is assigned to the interstitial region and is not accounted for in the ρ_α values.

The IPR is less sensitive to the size of the supercell, in contrast to the localization ratio. We obtain $\chi = 0.027$ for the VBE of a 128-atom GaAs:Bi supercell vs $\chi = 0.016$ in the reference 128-atom supercell of GaAs. In the case of a 432-atom supercell, the corresponding values are $\chi = 0.0095$ and 0.0046. In both cases the IPR increases by approximately a factor of 2 due to the disorder associated with the impurity.

B. Defect formation energy

The formation energy of isoelectronic neutral defects is calculated using the expression [35]

$$E^f[\underline{\mathrm{Ga}}\mathrm{As}\!:\!X] = E_{\mathrm{tot}}[\underline{\mathrm{Ga}}\mathrm{As}\!:\!X] - E_{\mathrm{tot}}[\mathrm{GaAs}] - \mu[X] + \mu[\mathrm{Ga}], \tag{5}$$

where E_{tot} is the DFT total energy and μ represents the chemical potential. The notation $\underline{\mathrm{Ga}}\mathrm{As}\!:\!X$ implies that the element X is substituted in place of a Ga atom in GaAs. In the calculations, the impurity is placed in a host 128-atom $4 \times 4 \times 4$ supercell, followed by relaxation of atomic positions while keeping the size of the cell constrained at the equilibrium value for GaAs.

Here, we assume a bulk source of impurities for B, Al, P, In, Sb, Tl, and Bi. The DFT total energy serves as an approximation for their chemical potential,

$$\mu[X] \approx E_{\mathrm{tot}}[X_{\mathrm{bulk}}]. \tag{6}$$

The nitrogen source is a N_2 molecule, with the chemical potential approximated by

$$\mu[\mathrm{N}] \approx \frac{1}{2} E_{\mathrm{tot}}[\mathrm{N}_2]. \tag{7}$$

By using DFT total energies for the chemical potential, we neglect the zero-point energy, the vibrational energy, and entropy, as well as the pressure contributions to the free energy. The chemical potential of Ga is considered within the uncertainty

$$E_{\mathrm{tot}}[\mathrm{GaAs}] - E_{\mathrm{tot}}[\mathrm{As}_{\mathrm{bulk}}] < \mu[\mathrm{Ga}] < E_{\mathrm{tot}}[\mathrm{Ga}_{\mathrm{bulk}}], \tag{8}$$

which corresponds to Ga-poor and Ga-rich growth conditions (the lower and upper bounds, respectively). The energy width of the range is determined by the formation enthalpy of the host lattice,

$$\Delta H_f[\mathrm{GaAs}] \approx E_{\mathrm{tot}}[\mathrm{GaAs}] - E_{\mathrm{tot}}[\mathrm{As}_{\mathrm{bulk}}] - E_{\mathrm{tot}}[\mathrm{Ga}_{\mathrm{bulk}}]. \quad (9)$$

We can rewrite Eq. (8) using the formation enthalphy as

$$E_{\mathrm{tot}}[\mathrm{Ga}_{\mathrm{bulk}}] + \Delta H_f[\mathrm{GaAs}] < \mu[\mathrm{Ga}] < E_{\mathrm{tot}}[\mathrm{Ga}_{\mathrm{bulk}}]. \quad (10)$$

It is straightforward to modify Eqs. (6)–(10) for the case of group-V-type defects, $\mathrm{Ga}\underline{\mathrm{As}}:X$.

The DFT total energies are obtained using the Vienna *ab initio* simulation program and projector augmented-wave potentials [36–38]. The Perdew-Burke-Ernzerhof (PBE) generalized-gradient approximation [39] for the exchange-correlation functional is utilized to maximize the chemical accuracy of the calculations. The cutoff energy for a plane-wave expansion is set at the level of 25% higher than the value recommended in pseudopotential files (215–500 eV, depending on the chemical composition). Our calculations yield the formation enthalpy of $\Delta H_f = -0.65$ eV per formula unit of GaAs. This result agrees reasonably well with the experimental value of -0.74 eV [40], giving the uncertainty of ± 0.03 eV/atom for reaction energies obtained with DFT PBE [41].

C. Special quasirandom alloys

The compound alloys are modeled as random unless otherwise specified in the text. Since there are multiple possible realizations of a random alloy structure, we use a special-quasirandom-structure (SQS) approach [42]. The alloy-theoretic automated toolkit package [43] is used to distribute alloying elements within the supercell of 128 atoms using the MCSQS code. The alloy state is characterized by an objective function that captures deviations of atomic correlation functions from the ideal random alloy. Our objective function includes pair, triplet, and quadruplet correlations with the cutoff distances of 8.1, 5.8, and 4.1 Å, respectively. The selection of cutoff distances corresponds to the fourth, second, and first nearest-neighbor atoms (respectively) on the same sublattice.

A metropolis Monte Carlo algorithm is utilized to minimize the objective function with a default annealing temperature. To assist the algorithm in finding a global minimum, ten differently seeded simulations are run, until convergence and the structure with the lowest objective function is chosen for the DFT calculations. Additional constraints are imposed in the SQS search algorithm to keep the supercell lattice vectors consistent with the primitive lattice and $4 \times 4 \times 4$ multiplicity.

III. RESULTS AND DISCUSSION

A. Isovalent substitutional impurities in GaAs

We begin by studying localization effects caused by isolated impurities in GaAs. The aim is to identify a single characteristic that captures chemical trends and therefore can serve as a prediction tool for mixing alloy elements into a host lattice. The electronegativity is a straightforward candidate to begin with. In the case of dilute nitrides, the localization is attributed to a large electronegativity difference between N and As [17] (3.04 vs 2.18 according to Pauling's scale [44]). On the other hand, Sb and Bi behave differently in GaAs, regardless of the nearly identical electronegativity values (2.05 vs 2.02).

The Born effective charge Z^* captures the ability of an atom to attract bonding electrons by taking into consideration the particular chemical environment. The results shown in Fig. 1 indicate that Bi in GaAs is significantly more electropositive than Sb, which translates into a greater impact of Bi on the electronic structure of GaAs. From all isovalent impurities in GaAs, nitrogen shows the most striking value of $Z^* \approx -6$, which is drastically different from the value of $Z^* = -2.7$ for nitrogen in GaN [45]. The effective charge of Tl suggests that it is the most electropositive group-III element, contrary to the fact that B and Tl have identical electronegativity values [44].

Calculations of the effective charge for supercells are computationally demanding. The trend line in Fig. 1 suggests that the Born effective charge scales linearly with sp^3-hybrid orbital energies obtained from Ref. [46] (p. 50), which can be used to predict the impact of an impurity on the electronic structure of the host lattice. A significance of the relative alignment of impurity-host orbital energies for the electronic stricture of alloys was previously pointed out

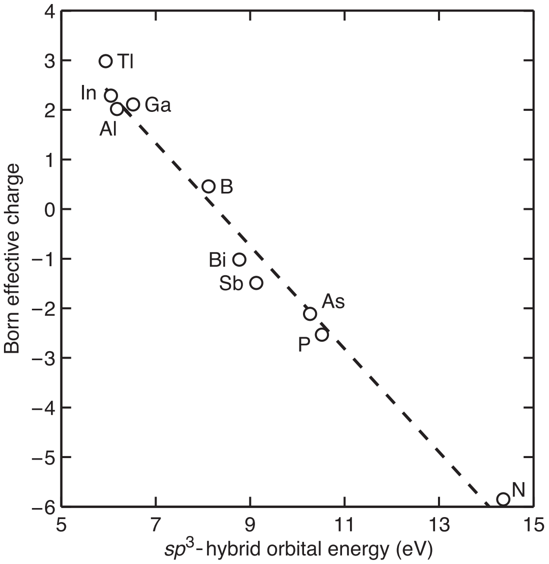

FIG. 1. Born effective charge for isovalent GaAs:X impurities as a function of their sp^3-hybrid orbital energy.

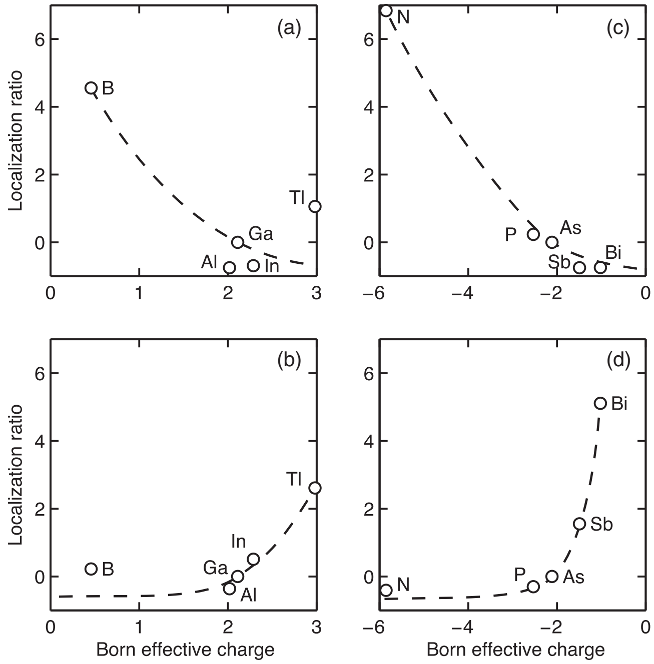

FIG. 2. Localization ratio defined by Eq. (1) for the electronic states at the (a),(c) conduction- and (b),(d) valence-band edges in GaAs due to single isovalent impurities plotted as a function of the element's Born effective charge. The dashed line is a guide for the eye.

TABLE III. Localization ratio ζ for single isovalent impurities compared to experimental values of the charge-carrier mobility μ and the PL linewidth (the full width at half maximum).

	PL linewidth	μ/μ_{GaAs} (%)		ζ	
Impurity	(meV)	electrons	holes	CBE	VBE
GaAs (host)	5^{a}	100^{b}	100^{c}	0	0
GaAs:B	$40{,}70^{d}$	⋯	⋯	4.56	0.22
GaAs:Al	4^{e}	96	96^{f}	−0.75	−0.36
GaAs:In	2–4, 10^{g}	$\gtrsim 100^{h}$	⋯	−0.69	0.51
GaAs:Tl	⋯	⋯	⋯	1.06	2.61
GaAs:N	30, 105^{i}	63^{j}	⋯	6.84	−0.41
GaAs:P	10^{k}	$\approx 100^{l}$	⋯	0.23	−0.30
GaAs:Sb	10, 23^{m}	≈100	25^{n}	−0.75	1.55
GaAs:Bi	64, 100^{o}	87	18^{p}	−0.74	5.11

[a] 2 K [49].

[b] Room temperature (Ref. [50], p. 91).

[c] Weakly doped room temperature [51].

[d] 1.6% B at 300 K, pump intensity 300 W/cm^2, bulklike [52], 3% B at 10 K excluding substrate [53].

[e] 2.9% Al, 2 K, pump intensity 10^{-3}–10 W/cm^2 (Ref. [54]).

[f] Room temperature 1.6% Al (Ref. [55], p. 626).

[g] $\mathrm{Ga}_{0.46}\mathrm{In}_{0.54}\mathrm{As}$ at 77 K [56], ≈1% In at 4.2 K at 10^{-3}–10 W/cm^2 (Ref. [57]).

[h] Room temperature [58].

[i] Annealed structure at 5 K at 2% average of 10 μW [59], 4 K at 1.4% [60].

[j] Room temperature [61].

[k] P 30% at 12 K quantum-well structure of ≈5 quantum wells 2.7 nm thick [57].

[l] Room temperature [62].

[m] Sb ≈ 6% at 4.2 K at (0.001–10) W/cm^2 (Ref. [57]), 4.4% Sb with excitation intensity of 2 W/cm^2 at 4 K [63].

[n] 8% Sb, room temperature [64].

[o] 2.6% Bi at 10 K [65], 1.3% at 9 K at 1 mW [66,67].

[p] Ref. [67].

by Deng *et al.* [21]. The orbital energies of the valence shells together with the overlap parameters are capable of capturing trap states and localization effects in various alloys, as demonstrated by O'Reilly's group from a tight-binding perspective [47,48].

Figure 2 shows the localization in CBEs and VBEs due to isovalent impurities in GaAs. Among all impurities, nitrogen introduces the strongest localization, followed by Bi and B. Those elements have more than a $1e$ difference in the Born effective charge with respect to the host elements they are substituted for. The localization ratio due to Tl and Sb is at an intermediate level. As one would expect, elements with a lower Born effective charge are effective in capturing electrons, thus introducing localized states in the conduction band. The opposite applies to the valence band.

Signatures of the electron localization can be observed via a broadening of the low-temperature PL linewidth as well as a deterioration of the transport coefficients. The available experimental data for ternary alloys are gathered in Table III alongside the calculated values of the localization ratio. Based on these data, we can suggest a criterion of the localization ratio $\zeta \lesssim 1$ for impurities that virtually do not impede charge-carrier transport. This guideline can be used in alloy design for applications where the charge transport plays a crucial role, e.g., photovoltaics where a high-mobility, bipolar charge-carrier transport is desired.

The ability of an individual element to change the band gap also scales with the localization ratio. Figure 3(a) shows the change of a band gap of GaAs due to the single impurity, which corresponds to an effective concentration of 1.6% in the 128-atom supercell with a TBMBJ [29] potential. Nitrogen is by far the most effective alloying element from the band-gap-reduction point of view, followed by Bi, B, and Sb. The band-gap reduction occurs by either lowering the conduction band or shifting up the valence-band edge, depending on which band edge is primarily affected by the disorder [Fig. 3(b)]. It is the conduction band for N and B and, conversely, the valence band for Bi and Tl (see Table III). These general results are consistent with known trends for dilute nitrides [10] and bismides [68]. This information is relevant for the band-gap engineering in semiconductor heterostructures, where the quantum carrier confinement is a design parameter.

The practical implementation of compound semiconductor alloys is associated with challenges related to their formability. Growth of metastable alloys is a complex process that is largely driven by kinetic effects at the surface, rather than by thermodynamic potentials of the bulk material. A notable example is the incorporation of Bi or N in GaAs that is possible to achieve experimentally at a

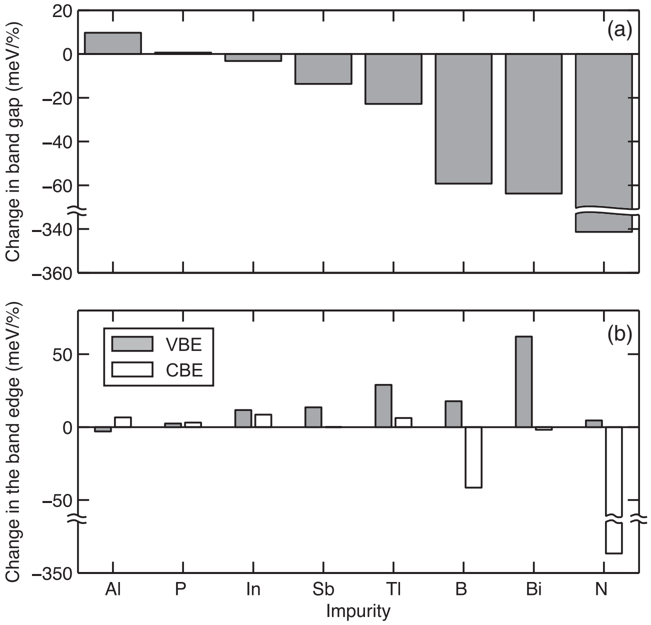

FIG. 3. Effect of single impurities on (a) the band gap and (b) the relative alignment of the band edges in GaAs.

level which exceeds their predicted solubility by several orders of magnitude [69,70]. Although the defect formation enthalpy presented in Fig. 4 cannot be directly related to the solubility, it can still serve as a guideline for evaluating formability of the alloys. Based on these data, one would expect the growth of dilute borides to pose more challenges than thallides or bismides. The energy penalty associated with incorporation of nitrogen in GaAs is at an intermediate level among other group-III-V elements. These results can be understood as an interplay between the chemical bond and local strain energies. The formation enthalpy of BAs is −0.31 eV [71] per formula unit, compared to −1.62 eV [72] for GaN. As a result, the strain energy due to the size mismatch between N and As is partly compensated for by the strong Ga—N bond, which is not the case for the B—As bond. The incorporation of Tl and Bi in GaAs is hindered for the same reason. It is instructive to note that the energy penalty associated with incorporation of a group-III-V element in GaAs (Fig. 4) is not always leveraged through the efficient band-gap reduction or the effective quantum-confinement engineering for semiconducting heterostructures (Fig. 3).

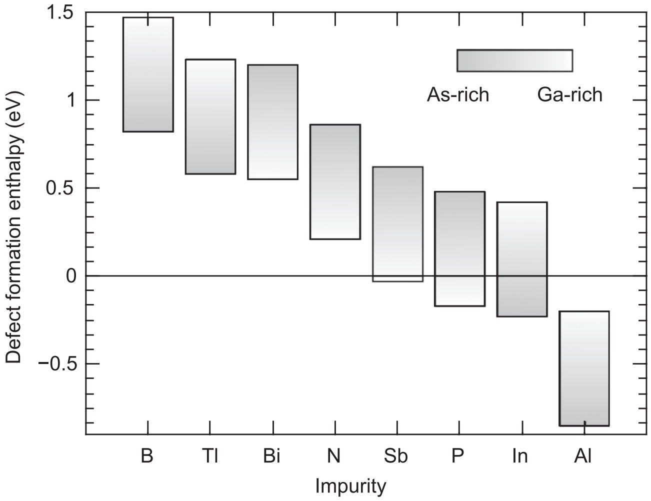

FIG. 4. Formation enthalpy of isovalent substitutional defects in a GaAs host lattice. The lower the enthalpy, the more preferred the impurity is in the host system. The range of energies is linked to the growth conditions that are encoded in the gradient fill.

B. Semiconductor alloys for telecommunication lasers

1. $In_{0.53}Ga_{0.47}As$

Extending the preceding impurity study to alloys, we show the link between localization characteristics, the band structure, and properties of gain materials for telecommunication lasers with an emission wavelength of 1.55 μm. We begin with the $In_{0.53}Ga_{0.47}As$ alloy, which represents the first generation of gain materials. The effective band structure is shown in Fig. 5(a). The calculated band gap of 0.79 eV agrees well with the targeted emission wavelength. The Bloch character is well preserved in the vicinity of the band edges and persists approximately 0.5 eV into the bands. The light and heavy hole bands, as well as the split-off band, are clearly resolved on the unfolded band structure. The conduction band at the L valley is energetically well isolated from the Γ valley that prevents spurious interactions and mixing between these states in the alloy.

The above-noted features of the effective alloy band structure are consistent with the narrow low-temperature PL linewidth (2–4 meV, Ref. [56]), the high mobility of electrons (20 000–80 000 $cm^2\,V^{-1}\,s^{-1}$, Refs. [56,73]) and holes (600–1000 $cm^2\,V^{-1}\,s^{-1}$, Refs. [74,75]) observed experimentally in $In_xGa_{1-x}As$, with $x \approx 0.5$. A very narrow (0.34 meV) intrinsic broadening of the band-edge alloy state in the $In_{0.5}Ga_{0.5}P$ alloy are predicted based on empirical potential calculations [76]. The low value of the localization ratio ($\zeta < 1$) for GaAs:In impurities is consistent with these observations. Therefore, $In_{0.53}Ga_{0.47}As$ can be viewed as a nearly disorder-free alloy.

The density of states and the IPR spectrum for the $In_{0.53}Ga_{0.47}As$ alloy are plotted in Fig. 6(a). The magnitude of IPR at the band edges is very close to its disorder-free limit of $\chi = 1/64$, which corresponds to the 128-atom supercell. States with a higher excess kinetic energy in the valence and conduction bands show a slight increase of the IPR, particularly in the conduction band when the energy approaches the L valley ($E \approx 1.4$ eV). These states do not contribute to inhomogeneous broadening of the optical gain and do not hamper the charge-carrier transport coefficients. However, states with the kinetic energy $E_k \approx E_g$ are involved in the Auger recombination, which is an important

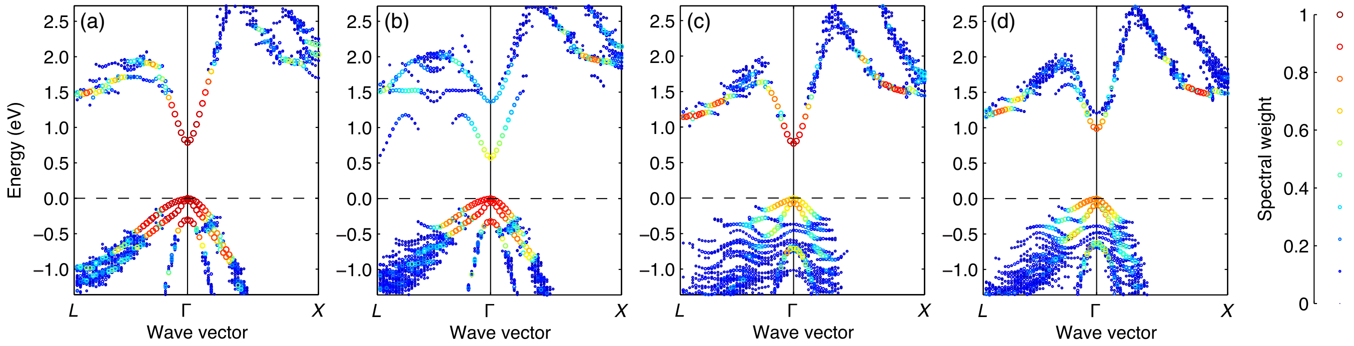

FIG. 5. Effective band structure of semiconductor alloys for telecommunication lasers with an emission wavelength of 1.55 μm. (a) $In_{0.53}Ga_{0.47}As$. (b) $In_{0.41}Ga_{0.59}N_{0.03}As_{0.94}Sb_{0.03}$. (c) $GaAs_{0.89}Bi_{0.11}$. (d) $Ga_{0.91}B_{0.09}As_{0.89}Bi_{0.11}$. The origin of the energy scale is set at the Fermi energy. The legend on the right shows the Bloch spectral weight. Only data points with a spectral weight of 5% of greater are shown.

loss mechanism for lasers. Implications of the disorder for the Auger recombination are discussed below.

2. $In_{0.41}Ga_{0.59}N_{0.03}As_{0.94}Sb_{0.03}$

Dilute nitride semiconductors represent the second generation of gain materials designed for an emission wavelength of 1.55 μm and a monolithic integration on a GaAs substrate [77]. The effective band structure of $In_{0.41}Ga_{0.59}N_{0.03}As_{0.94}Sb_{0.03}$ is illustrated in Fig. 5(b). The enhanced statistics of In—N bonds is incorporated into the atomistic structure to model the effect of annealing on material characteristics. The Bloch character in the valence band structure remains well defined similar to (In,Ga)As, which corresponds with a similar IPR spectrum [Figs. 6(b)]. The CBE has drastically changed from (In,Ga)As. The retention of its Γ character is only about 50% [Fig. 5(b)], which is accompanied by the abrupt increase of the IPR (i.e., localization) within the conduction band and near the edge [Fig. 6(b)]. It is worth noting that the strength of localization in the conduction band *increases* with increasing the electron excess energy, contrary to the common view based on the classical Anderson model of localization. The largest IPR value of nearly 0.06 can be interpreted as an orbital wave function being localized in the vicinity of $0.06^{-1} \approx 17$ atoms only. This observation is consistent with the low Bloch character (less than 30%) for states within the energy window $E = 1.0$–1.3 eV [Fig. 5(b)].

These features of the electronic structure of dilute nitrides lead to a broadening of the PL linewidth (18–40 meV, Refs. [8,77–79]) and a reduction of the electron mobility (100 $cm^2\,V^{-1}\,s^{-1}$, Ref. [80]), whereas the hole mobility remains unaffected (900 $cm^2\,V^{-1}\,s^{-1}$, Ref. [80]). These observations also conform with the single-impurity (GaAs:N and GaAs:Sb) localization studies presented in the preceding subsection. One can anticipate a detrimental impact of localization at the CBE on the optical gain in this material system. The reason for an intrinsic "disorder penalty" is twofold: (i) smearing of the Bloch character impedes the k-selection rules for the optical transition and reduces the dipole matrix element, and (ii) the inhomogeneous broadening reduces the gain.

3. $GaAs_{0.89}Bi_{0.11}$

We now turn to the third generation of the gain materials, namely, dilute bismide $GaAs_{1-x}Bi_x$ alloys. Their development is inspired by a potential ability to reduce the Auger losses [81]. The bismuth content of $x = 0.11$ is selected to match an anticipated band gap with an emission wavelength of 1.55 μm [13]. The band structure of $GaAs_{0.89}Bi_{0.11}$ is shown in Fig. 5(c). Contrary to the dilute nitrides, the bismides demonstrate a well-defined profile in the conduction band, whereas the valence band is severely distorted [20,32]. The conduction-band minimum is well resolved, with a strong Γ character without a noticeable mixing with L and X states. The split-off band is located at $\Delta_{SO} = 0.72$ eV below the valence-band edge. At such a high bismuth content, the spin-orbit splitting approaches the band gap, which is $E_g = 0.77$ eV in our case ($\Delta_{SO} > E_g$ is desired for a suppression of the Auger recombination). In both material systems, (In,Ga)As and (Ga,In)(N,As,Sb), which are studied above, this condition is far from being fulfilled.

Examining the localization effects in $GaAs_{0.89}Bi_{0.11}$ [Fig. 6(c)], we discern that states at the valence-band edge have a degree of localization comparable to (Ga,In)(N,As,Sb) alloys. These results explain the broad low-temperature PL linewidth of Ga(As,Bi) alloys (60–70 meV, Refs. [82,83]) and the steep decline of the hole mobility (6–15 $cm^2\,V^{-1}\,s^{-1}$, Refs. [67,84]). Dilute bismides exhibit stronger localization effects than dilute nitrides, even though the localization in GaAs:Bi is less pronounced at the single-impurity level than in GaAs:N ($\zeta_{Bi}^{VBE} < \zeta_{N}^{CBE}$; see Table III). The enhanced localization in dilute bismides can be attributed to the much higher concentration of bismuth, which is required to achieve the same band-gap reduction as in dilute nitrides. Accordingly, the alloy statistics leads to

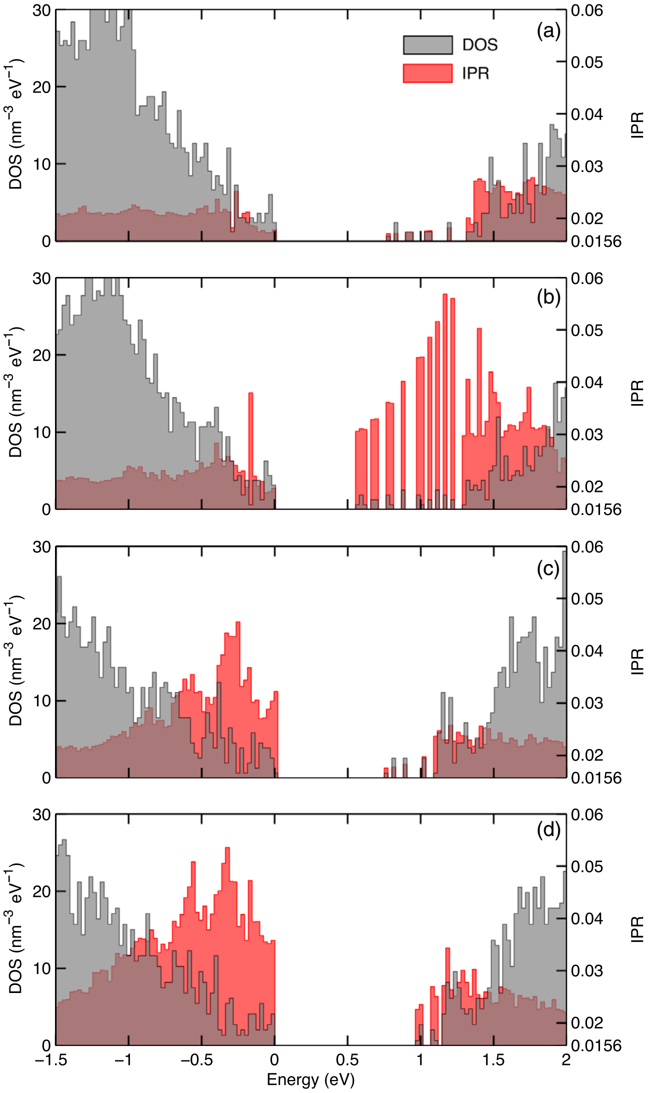

FIG. 6. Density of states (DOS) shown alongside the inverse participation ratio (IPR), which captures the strength of localization in semiconductor alloys for telecommunication lasers with the emission wavelength of 1.55 μm. (a) $In_{0.53}Ga_{0.47}As$. (b) $In_{0.41}Ga_{0.59}N_{0.03}As_{0.94}Sb_{0.03}$. (c) $GaAs_{0.89}Bi_{0.11}$. (d) $Ga_{0.91}B_{0.09}As_{0.89}Bi_{0.11}$. The lower limit of IPR 1/64 corresponds to pure Bloch states in the 128-atom supercell.

a higher probability of forming pairs (Bi-Ga-Bi) and higher-order clusters, which have a detrimental effect on the electronic structure at the VBE [20,48].

The above discussion of the disorder penalty and its impact on gain characteristics is fully applicable to the Ga(As,Bi) material system. The disorder also has implications on optical losses. The Auger recombination is a many-particle process, the likelihood of which is determined by the energy and momentum (wave-vector) conservation of the electronic states involved. In materials with strong disorder, the momentum-conservation requirement is relaxed due to uncertainties of the wave vector **k** inherent to localized states. Therefore, the inferred reduction of Auger losses in Ga(As,Bi) gain media requires a thorough analysis, which will take into account the realistic band structure shown in Fig. 5(c) and the presence of alloy disorder.

4. $Ga_{0.91}B_{0.09}As_{0.89}Bi_{0.11}$

Finally, we would like to comment on quaternary bismide alloys. For instance, the Ga(N,As,Bi) material system [81,85] offers an additional flexibility in engineering of the lattice mismatch and/or band offsets. Here, we study a $Ga_{0.91}B_{0.09}As_{0.89}Bi_{0.11}$ alloy, which is inspired by the physics of In—N bonds in (Ga,In)(N,As) [18,86]. One would expect that the incorporation of boron will further reduce the band gap and help to mitigate the local strain fields by forming B—Bi bonds (a correlated alloy). By contrast, the addition of boron results in an upward shift of the Γ valley of the conduction band and an opening of the band gap [Fig. 5(d)]. This result suggests that the properties of quaternary alloys are governed by more-complicated physics than a simple additive effects of ternary compounds. The positive effect of boron is an improvement of the Bloch character of the VBE [Fig. 5(d)] compared to the boron-free alloy [Fig. 5(c)]. However, there are two drawbacks: (i) a more-severe localization develops in the conduction band and deeper energy states in the valence band, and (ii) the incorporation of boron in a GaAs lattice can be challenging due to the high defect formation energy (Fig. 4). Nevertheless, (Ga,B)(As,Bi) could be an alternative material system for multijunction solar cells with a 1-eV band gap and lattice matched to GaAs.

It is important to note that the results presented above are obtained for bulk materials, which does not take into account an epitaxial strain that can arise from a lattice mismatch between the layer and the substrate. The strain is not an issue for $In_{0.53}Ga_{0.47}As$ and $Ga_{0.91}B_{0.09}As_{0.89}Bi_{0.11}$ alloys, as their lattice constant is intended to match the substrates, InP and GaAs, respectively. By contrast, $In_{0.41}Ga_{0.59}N_{0.03}As_{0.94}Sb_{0.03}$ and $GaAs_{0.89}Bi_{0.11}$ alloys possess a lattice mismatch of 2.6% and 1.4% with respect to GaAs (see the theoretical lattice parameters in Tables I and II). Two methods, namely, Matthews and Blakeslee [87] and Voisin [88], are used to assess a critical thickness h_c of the film that can accommodate the epitaxial strain elastically without generating misfit dislocations. Both approaches produce similar results of $h_c = 2.5$ nm for $In_{0.41}Ga_{0.59}N_{0.03}As_{0.94}Sb_{0.03}/GaAs$ and 6 nm for $GaAs_{0.89}Bi_{0.11}/GaAs$ heterostructures. Layers with a thickness less than h_c will be tetragonally distorted, which may have an additional impact on localization characteristics. We evaluate the effect of a tetragonal distortion on the electronic structure and localization in the compressively strained $GaAs_{0.89}Bi_{0.11}$ compound on a GaAs substrate (see the Appendix). The tetragonal distortion leads to an opening of the band gap and a lifting of the degeneracy between heavy and light holes, which is consistent with effects expected from a compressive in-plane strain of the layer [88]. There are no major changes observed in the IPR spectrum, indicating that the alloy disorder is not sensitive to the epitaxial strain for the particular material system and the strain magnitude.

IV. CONCLUSIONS

DFT calculations are used to perform a systematic characterization of isovalent impurities (B, N, Al, P, In, Sb, Tl, and Bi) in the host GaAs. The degree of localization present in electronic states near the band edges decreases in the following order: N, Bi, B, Tl, and Sb. Other elements do not cause a notable localization of the electronic states. The localization strength scales with the Born effective charge, which is calculated for individual impurities. The effective charge of impurities can be markedly different from their nominal values in binary compounds reflecting their electropositive or electronegative nature in the specific host lattice. Elements which have a Born effective charge less than the host introduce localized states in the conduction band but do not perturb the valence-band edge, and vice versa. The extremity of localization at the band edges directly correlates with several important characteristics, such as the charge-carrier transport, broadening of the photoluminescence spectra, the ability of individual elements to change the band gap, and the relative band alignment. An extensive comparison with experimental data gives confidence in the predictive power of first-principles calculations. The energy penalty associated with incorporation of impurities in the host lattice does not follow the localization pattern and decreases in the following order: B, Tl, Bi, N, and Sb. This result implies that the growth of dilute borides poses more challenges than thallides or bismides. The incorporation of nitrogen in GaAs is assisted by the strong Ga—N bond.

We perform a comparative study of localization in (In,Ga)As, (Ga,In)(N,As,Sb) and Ga(As,Bi) compound alloys, which represent three generations of material systems for telecommunication lasers. A wave-function inverse participation ratio calculated for individual eigenstates is used as a measure for the extremity of localization. The results indicate that the electronic structure of (In,Ga)As is least affected by the alloy disorder. The electronic states near the conduction-band edge of (Ga,In)(N,As,Sb) and the valence-band edges of Ga(As,Bi) are strongly affected by the disorder. The extremity of localization at the valence-band edge of Ga(As,Bi) is approximately 2 times greater than that for the conduction-band edge of (Ga,In)(N,As,Sb). This result translates into an intrinsically higher inhomogeneous broadening inherent to dilute bismide alloys compared to their dilute nitride counterparts, which can have an unfavorable impact on the optical gain characteristics and Auger losses. This conclusion should not be extended to group-III antimonide semiconductors alloyed with Bi for midinfrared devices. The smaller electronic difference between Sb and Bi should lead to a less detrimental impact of Bi on the structure of (Al,Ga,In)(Sb,Bi), according to the arguments presented above for single impurities.

ACKNOWLEDGMENTS

The authors are thankful to Axel van de Walle and Joseph Zwanziger for the helpful discussions regarding the generation of quasirandom structures, as well as to Maciej Polak for the critical reading of the manuscript. Funding is provided by the Natural Sciences and Engineering Research Council of Canada under Discovery Grant Program No. RGPIN-2015-04518. This work was performed using computational resources of the Thunder Bay Regional Research Institute, Lakehead University, and Compute Canada (Calcul Quebec).

APPENDIX: EFFECT OF THE EPITAXIAL STRAIN (TETRAGONAL DISTORTION)

The effect of epitaxial strain on the electronic structure of $GaAs_{0.89}Bi_{0.11}$ is studied using a 128-atom supercell. The lattice parameters in lateral directions (a_c and b_c) are fixed to that of GaAs [Fig. 7(a)]; the c_c lattice constant remains unconstrained. The lattice parameters and angles of the rhombohedral primitive cell are scaled to reproduce the tetragonal lattice distortion, as shown in Fig. 7(a).

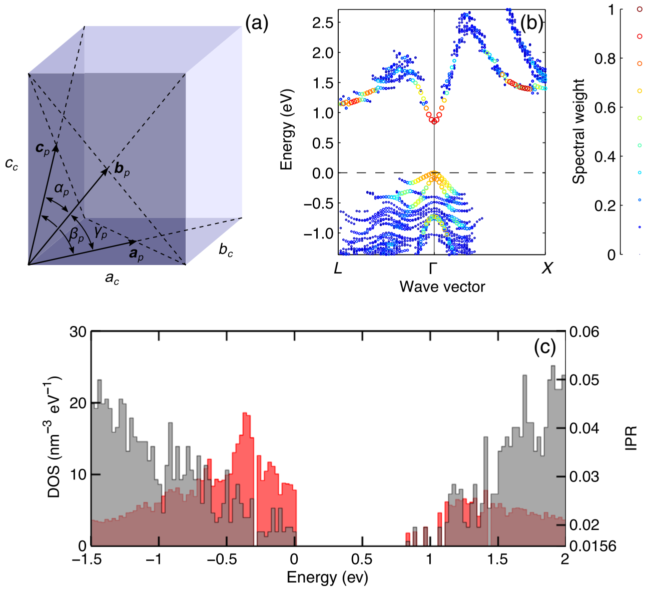

FIG. 7. Effect of epitaxial strain on the electronic structure of $GaAs_{0.89}Bi_{0.11}$. (a) Conventional unit cell with a tetragonal distortion in relation to the primitive lattice vectors $\mathbf{a}_p$, $\mathbf{b}_p$, and $\mathbf{c}_p$, and angles. (b) Unfolded band structure. The wave vectors are selected within the growth plane (001). (c) Density of states (DOS) and the inverse participation ratio (IPR). The origin of the energy scale is set at the Fermi energy.

The most noticeable changes in the electronic structure of $GaAs_{0.89}Bi_{0.11}$ due to the epitaxial strain are an opening of the band gap by approximately 0.1 eV and a lifting up of the degeneracy at the top of the valence band [Fig. 7(b)]. The Bloch character, the density of states, and localization characteristics assessed via the inverse participation ratio do not show any prominent changes compared to the bulk material [Figs. 5(c) and 6(c)].

[1] Masafumi Yamaguchi, Tatsuya Takamoto, Kenji Araki, and Nicholas Ekins-Daukes, Multi-junction III–V solar cells: Current status and future potential, Solar Energy **79**, 78 (2005).

[2] Chaturvedi Gogineni, Nathaniel A. Riordan, Shane R. Johnson, Xianfeng Lu, and Tom Tiedje, Disorder and the Urbach edge in dilute bismide GaAsBi, Appl. Phys. Lett. **103**, 041110 (2013).

[3] Igor P. Marko, Christopher A. Broderick, Shirong Jin, Peter Ludewig, Wolfgang Stolz, Kerstin Volz, Judy M. Rorison, Eoin P. O'Reilly, and Stephen J. Sweeney, Optical gain in GaAsBi/GaAs quantum well diode lasers, Sci. Rep. **6**, 28863 (2016).

[4] C. A. Broderick, M. Usman, S. J. Sweeney, and E. P. O'Reilly, Band engineering in dilute nitride and bismide semiconductor lasers, Semicond. Sci. Technol. **27**, 094011 (2012).

[5] Masahiko Kondow, Kazuhisa Uomi, Atsuko Niwa, Takeshi Kitatani, Seiji Watahiki, and Yoshiaki Yazawa, GaInNAs: A novel material for long-wavelength-range laser diodes with excellent high-temperature performance, Jpn. J. Appl. Phys. **35**, 1273 (1996).

[6] M. Kneissl, T. Kolbe, C. Chua, V. Kueller, N. Lobo, J. Stellmach, A. Knauer, H. Rodriguez, S. Einfeldt, Z. Yang, N. M. Johnson, and M. Weyers, Advances in group III-nitride-based deep UV light-emitting diode technology, Semicond. Sci. Technol. **26**, 014036 (2011).

[7] K. Alberi, J. Wu, W. Walukiewicz, K. M. Yu, O. D. Dubon, S. P. Watkins, C. X. Wang, X. Liu, Y.-J. Cho, and J. Furdyna, Valence-band anticrossing in mismatched III–V semiconductor alloys, Phys. Rev. B **75**, 045203 (2007).

[8] O. Rubel, M. Galluppi, S. D. Baranovskii, K. Volz, L. Geelhaar, H. Riechert, P. Thomas, and W. Stolz, Quantitative description of disorder parameters in (GaIn)(NAs) quantum wells from the temperature-dependent photoluminescence spectroscopy, J. Appl. Phys. **98**, 063518 (2005).

[9] T. Tiedje, E. C. Young, and A. Mascarenhas, Growth and properties of the dilute bismide semiconductor $GaAs_{1-x}Bi_x$ a complementary alloy to the dilute nitrides, Int. J. Nanotechnology **5**, 963 (2008).

[10] P. R. C. Kent and A. Zunger, Theory of electronic strucuture evolution in GaAsN and GaPN alloys, Phys. Rev. B **64**, 115208 (2001).

[11] Yong Zhang, A. Mascarenhas, and L.-W. Wang, Similar and dissimilar aspects of III–V semiconductors containing Bi versus N, Phys. Rev. B **71**, 155201 (2005).

[12] Yong Zhang, A. Mascarenhas, and L.-W. Wang, Systematic approach to distinguishing a perturbed host state from an impurity state in a supercell calculation for a doped semiconductor: Using GaP:N as an example, Phys. Rev. B **74**, 041201 (2006).

[13] A. R. Mohmad, F. Bastiman, C. J. Hunter, R. D. Richards, S. J. Sweeney, J. S. Ng, J. P. R. David, and B. Y. Majlis, Localization effects and band gap of GaAsBi alloys, Phys. Status Solidi B **251**, 1276 (2014).

[14] Weng W. Chow and Stephan W. Koch, *Semiconductor-Laser Fundamentals: Physics of the Gain Materials* (Springer Science+Business Media, New York, 1999).

[15] E. Fred Schubert and Jong Kyu Kim, Solid-state light sources getting smart, Science **308**, 1274 (2005).

[16] S. V. Dudiy and Alex Zunger, Searching for Alloy Configurations with Target Physical Properties: Impurity Design via a Genetic Algorithm Inverse Band Structure Approach, Phys. Rev. Lett. **97**, 046401 (2006).

[17] L. Bellaiche, S. H. Wei, and Alex Zunger, Localization and percolation in semiconductor alloys: GaAsN vs GaAsP, Phys. Rev. B **54**, 17568 (1996).

[18] P. J. Klar, H. Grüning, J. Koch, S. Schäfer, K. Volz, W. Stolz, W. Heimbrodt, A. M. Kamal Saadi, A. Lindsay, and E. P. O'Reilly, (Ga,In)(N,As)-fine structure of the band gap due to nearest-neighbor configurations of the isovalent nitrogen, Phys. Rev. B **64**, 121203(R) (2001).

[19] Muhammad Usman, Christopher A. Broderick, Zahida Batool, Konstanze Hild, Thomas J. C. Hosea, Stephen J. Sweeney, and Eoin P. O'Reilly, Impact of alloy disorder on the band structure of compressively strained $GaBi_xAs_{1-x}$, Phys. Rev. B **87**, 115104 (2013).

[20] Lars C. Bannow, Oleg Rubel, Stefan C. Badescu, Phil Rosenow, Jörg Hader, Jerome V. Moloney, Ralf Tonner, and Stephan W. Koch, Configuration dependence of band-gap narrowing and localization in dilute $GaAs_{1-x}Bi_x$ alloys, Phys. Rev. B **93**, 205202 (2016).

[21] Hui-Xiong Deng, Jingbo Li, Shu-Shen Li, Haowei Peng, Jian-Bai Xia, Lin-Wang Wang, and Su-Huai Wei, Band crossing in isovalent semiconductor alloys with large size mismatch: First-principles calculations of the electronic structure of Bi and N incorporated GaAs, Phys. Rev. B **82**, 193204 (2010).

[22] P. W. Anderson, Absence of diffusion in certain random lattices, Phys. Rev. **109**, 1492 (1958).

[23] Franz Wegner, Inverse participation ratio in $2+\varepsilon$ dimensions, Z. Phys. B **36**, 209 (1980).

[24] Bernhard Kramer and Angus MacKinnon, Localization: Theory and experiment, Rep. Prog. Phys. **56**, 1469 (1993).

[25] W. Kohn and L. J. Sham, Self-consistent equations including exchange and correlation effects, Phys. Rev. **140**, A1133 (1965).

[26] P. Blaha, K. Schwarz, G. K. H. Madsen, D. Kvasnicka, and J. Luitz, *WIEN2K: An Augmented Plane Wave+Local Orbitals Program for Calculating Crystal Properties* (Technische Universität Wien, Austria, 2001).

[27] H. J. Monkhorst and J. D. Pack, Special points for Brillouin-zone integrations, Phys. Rev. B **13**, 5188 (1976).

[28] Zhigang Wu and R. E. Cohen, More accurate generalized gradient approximation for solids, Phys. Rev. B **73**, 235116 (2006).

[29] Fabien Tran and Peter Blaha, Accurate Band Gaps of Semiconductors and Insulators with a Semilocal

Exchange-Correlation Potential, Phys. Rev. Lett. **102**, 226401 (2009).

[30] I. Vurgaftman, J. R. Meyer, and L. R. Ram-Mohan, Band parameters for III–V compound semiconductors and their alloys, J. Appl. Phys. **89**, 5815 (2001).

[31] I. Vurgaftman and J. R. Meyer, Band parameters for nitrogen-containing semiconductors, J. Appl. Phys. **94**, 3675 (2003).

[32] O. Rubel, A. Bokhanchuk, S. J. Ahmed, and E. Assmann, Unfolding the band structure of disordered solids: From bound states to high-mobility Kane fermions, Phys. Rev. B **90**, 115202 (2014).

[33] S. J. Ahmed, J. Kivinen, B. Zaporzan, L. Curiel, S. Pichardo, and O. Rubel, BERRYPI: A software for studying polarization of crystalline solids with WIEN2K density functional all-electron package, Comput. Phys. Commun. **184**, 647 (2013).

[34] N. C. Murphy, R. Wortis, and W. A. Atkinson, Generalized inverse participation ratio as a possible measure of localization for interacting systems, Phys. Rev. B **83**, 184206 (2011).

[35] Christoph Freysoldt, Blazej Grabowski, Tilmann Hickel, Jörg Neugebauer, Georg Kresse, Anderson Janotti, and Chris G. Van de Walle, First-principles calculations for point defects in solids, Rev. Mod. Phys. **86**, 253 (2014).

[36] Georg Kresse and Jürgen Furthmüller, Efficient iterative schemes for *ab initio* total-energy calculations using a plane-wave basis set, Phys. Rev. B **54**, 11169 (1996).

[37] G. Kresse and D. Joubert, From ultrasoft pseudopotentials to the projector augmented-wave method, Phys. Rev. B **59**, 1758 (1999).

[38] P. E. Blöchl, Projector augmented-wave method, Phys. Rev. B **50**, 17953 (1994).

[39] John P. Perdew, Kieron Burke, and Matthias Ernzerhof, Generalized Gradient Approximation Made Simple, Phys. Rev. Lett. **77**, 3865 (1996).

[40] Mohamed Tmar, Armand Gabriel, Christian Chatillon, and Ibrahim Ansara, Critical analysis and optimization of the thermodynamic properties and phase diagrams of the III–V compounds II. The Ga-As and In-As systems, J. Cryst. Growth **69**, 421 (1984).

[41] Geoffroy Hautier, Shyue Ping Ong, Anubhav Jain, Charles J. Moore, and Gerbrand Ceder, Accuracy of density functional theory in predicting formation energies of ternary oxides from binary oxides and its implication on phase stability, Phys. Rev. B **85**, 155208 (2012).

[42] Alex Zunger, S.-H. Wei, L. G. Ferreira, and James E. Bernard, Special Quasirandom Structures, Phys. Rev. Lett. **65**, 353 (1990).

[43] A. Van de Walle, P. Tiwary, M. De Jong, D. L. Olmsted, M. Asta, A. Dick, D. Shin, Y. Wang, L.-Q. Chen, and Z.-K. Liu, Efficient stochastic generation of special quasirandom structures, CALPHAD: Comput. Coupling Phase Diagrams Thermochem. **42**, 13 (2013).

[44] A. L. Allred, Electronegativity values from thermochemical data, J. Inorg. Nucl. Chem. **17**, 215 (1961).

[45] A. R. Goñi, H. Siegle, K. Syassen, C. Thomsen, and J.-M. Wagner, Effect of pressure on optical phonon modes and transverse effective charges in GaN and AlN, Phys. Rev. B **64**, 035205 (2001).

[46] W. A. Harrison, *Electronic Structure and Properties of Solids* (Dover, New York, 1989).

[47] A. Lindsay and E. P. O'Reilly, Unification of the Band Anticrossing and Cluster-State Models of Dilute Nitride Semiconductor Alloys, Phys. Rev. Lett. **93**, 196402 (2004).

[48] Muhammad Usman, Christopher A. Broderick, Andrew Lindsay, and Eoin P. O'Reilly, Tight-binding analysis of the electronic structure of dilute bismide alloys of GaP and GaAs, Phys. Rev. B **84**, 245202 (2011).

[49] E. Hal Bogardus and H. Barry Bebb, Bound-exciton, free-exciton, band-acceptor, donor-acceptor, and Auger recombination in GaAs, Phys. Rev. **176**, 993 (1968).

[50] J. D. Wiley, in *Semiconductors and Semimetals*, Vol. 10, edited by R. K. Willardson and Albert Beer (Academic Press, New York, 1975), p. 91.

[51] G. E. Stillman, C. M. Wolfe, and J. O. Dimmock, Hall coefficient factor for polar mode scattering in *n*-type GaAs, J. Phys. Chem. Solids **31**, 1199 (1970).

[52] V. Gottschalch, G. Leibiger, and G. Benndorf, MOVPE growth of $B_xGa_{1-x}As$, $B_xGa_{1-x-y}In_yAs$, and $B_xAl_{1-x}As$ alloys on (001) GaAs, J. Cryst. Growth **248**, 468 (2003).

[53] R. Hamila, F. Saidi, P. H. Rodriguez, Laurent Auvray, Y. Monteil, and H. Maaref, Growth temperature effects on boron incorporation and optical properties of BGaAs/GaAs grown by MOCVD, J. Alloys Compd. **506**, 10 (2010).

[54] D. C. Reynolds, K. K. Bajaj, C. W. Litton, P. W. Yu, Jasprit Singh, W. T. Masselink, R. Fischer, and H. Morkoç, Determination of interfacial quality of GaAs-GaAlAs multi-quantum well structures using photoluminescence spectroscopy, Appl. Phys. Lett. **46**, 51 (1985).

[55] Michael Shur, *Physics of Semiconductor Devices* (Prentice-Hall, Englewood Cliffs, NJ, 1990).

[56] H. Protzmann, F. Höhnsdorf, Z. Spika, W. Stolz, E. O. Göbel, M. Müller, and J. Lorberth, Properties of $(Ga_{0.47}In_{0.53})As$ epitaxial layers grown by metalorganic vapor phase epitaxy (MOVPE) using alternative arsenic precursors, J. Cryst. Growth **170**, 155 (1997).

[57] W. C. Mitchel and P. W. Yu, Study of electronic levels in antimony and indium-doped gallium arsenide, J. Appl. Phys. **57**, 623 (1985).

[58] Otfried Madelung and Sadao Adachi, *Landolt-Börnstein: Numerical Data and Functional Relationships in Science and Technology* (Springer, New York, 2002).

[59] R. Kudrawiec, M. Latkowska, M. Baranowski, J. Misiewicz, L. H. Li, and J. C. Harmand, Photoreflectance, photoluminescence, and microphotoluminescence study of optical transitions between delocalized and localized states in $GaN_{0.02}As_{0.98}$, $Ga_{0.95}In_{0.05}N_{0.02}As_{0.98}$, and $GaN_{0.02}As_{0.90}Sb_{0.08}$ layers, Phys. Rev. B **88**, 125201 (2013).

[60] J. Plaza, J. L. Castaño, B. J. García, H. Carrère, and E. Bedel-Pereira, Temperature dependence of photoluminescence and photoreflectance spectra of dilute GaAsN alloys, Appl. Phys. Lett. **86**, 121918 (2005).

[61] S. Dhar, A. Mondal, and T. D. Das, Hall mobility and electron trap density in GaAsN grown by liquid phase epitaxy, Semicond. Sci. Technol. **23**, 015007 (2008).

[62] James J. Tietjen and James A. Amick, The preparation and properties of vapor-deposited epitaxial $GaAs_{1-x}P_x$ using arsine and phosphine, J. Electrochem. Soc. **113**, 724 (1966).

[63] D. Huang, J. Chyi, J. Klem, and Hadis Morkoc, Optical properties of molecular beam epitaxially grown $\mathrm{GaAs}_{1-x}\mathrm{Sb}_x$ $(0 < x < 0.5)$ on GaAs and InP substrates, J. Appl. Phys. **63**, 5859 (1988).

[64] C. R. Bolognesi, M. M. W. Dvorak, P. Yeo, X. G. Xu, and S. P. Watkins, InP/GaAsSb/InP double HBTs: A new alternative for InP-based DHBTs, IEEE Trans. Electron Devices **48**, 2631 (2001).

[65] Kunishige Oe, Characteristics of semiconductor alloy $\mathrm{GaAs}_{1-x}\mathrm{Bi}_x$, Jpn. J. Appl. Phys. **41**, 2801 (2002).

[66] S. Francoeur, S. Tixier, E. Young, T. Tiedje, and A. Mascarenhas, Bi isoelectronic impurities in GaAs, Phys. Rev. B **77**, 085209 (2008).

[67] R. N. Kini, A. J. Ptak, B. Fluegel, R. France, R. C. Reedy, and A. Mascarenhas, Effect of Bi alloying on the hole transport in the dilute bismide alloy $\mathrm{GaAs}_{1-x}\mathrm{Bi}_x$, Phys. Rev. B **83**, 075307 (2011).

[68] M. P. Polak, P. Scharoch, and R. Kudrawiec, First-principles calculations of bismuth induced changes in the band structure of dilute Ga-V-Bi and In-V-Bi alloys: Chemical trends versus experimental data, Semicond. Sci. Technol. **30**, 094001 (2015).

[69] S. B. Zhang and Su-Huai Wei, Nitrogen Solubility and Induced Defect Complexes in Epitaxial GaAs:N, Phys. Rev. Lett. **86**, 1789 (2001).

[70] Andreas Beyer, Wolfgang Stolz, and Kerstin Volz, Metastable cubic zinc-blende III/V semiconductors: Growth and structural characteristics, Prog. Cryst. Growth Charact. Mater. **61**, 46 (2015).

[71] H. Dumont and Y. Monteil, Some aspects on thermodynamic properties, phase diagram and alloy formation in the ternary system BAs-GaAs—Part I: Analysis of BAs thermodynamic properties, J. Cryst. Growth **290**, 410 (2006).

[72] M. R. Ranade, F. Tessier, A. Navrotsky, V. J. Leppert, S. H. Risbud, F. J. DiSalvo, and C. M. Balkas, Enthalpy of formation of gallium nitride, J. Phys. Chem. B **104**, 4060 (2000).

[73] Yoshikazu Takeda, Akio Sasaki, Yujiro Imamura, and Toshinori Takagi, Electron mobility and energy gap of $\mathrm{In}_{0.53}\mathrm{Ga}_{0.47}\mathrm{As}$ on InP substrate, J. Appl. Phys. **47**, 5405 (1976).

[74] M. Sotoodeh, A. H. Khalid, and A. A. Rezazadeh, Empirical low-field mobility model for III–V compounds applicable in device simulation codes, J. Appl. Phys. **87**, 2890 (2000).

[75] P. S. Menon, K. Kandiah, and S. Shaari, Concentration and temperature-dependent low-field mobility model for $\mathrm{In}_{0.53}\mathrm{Ga}_{0.47}\mathrm{As}$ interdigitated lateral pin PD, IEICE Electron. Express **5**, 303 (2008).

[76] Yong Zhang and Lin-Wang Wang, Global electronic structure of semiconductor alloys through direct large-scale computations for III–V alloys $\mathrm{Ga}_x\mathrm{In}_{1-x}\mathrm{P}$, Phys. Rev. B **83**, 165208 (2011).

[77] Seth R. Bank, Hopil Bae, Lynford L. Goddard, Homan B. Yuen, Mark A. Wistey, Robert Kudrawiec, and James S. Harris, Recent progress on 1.55-μm dilute-nitride lasers, IEEE J. Quantum Electron. **43**, 773 (2007).

[78] Seth R. Bank, Mark A. Wistey, Lynford L. Goddard, Homan B. Yuen, Vincenzo Lordi, and James S. Harris, Jr., Low-threshold continuous-wave 1.5-μm GaInNAsSb lasers grown on GaAs, IEEE J. Quantum Electron. **40**, 656 (2004).

[79] Lynford L. Goddard, Seth R. Bank, Mark A. Wistey, Homan B. Yuen, Zhilong Rao, and James S. Harris, Recombination, gain, band structure, efficiency, and reliability of 1.5-μm GaInNAsSb/GaAs lasers, J. Appl. Phys. **97**, 083101 (2005).

[80] K. Volz, J. Koch, B. Kunert, and W. Stolz, Doping behaviour of Si, Te, Zn and Mg in lattice-matched (GaIn)(NAs)/GaAs bulk films, J. Cryst. Growth **248**, 451 (2003).

[81] S. J. Sweeney and S. R. Jin, Bismide-nitride alloys: Promising for efficient light emitting devices in the near- and mid-infrared, J. Appl. Phys. **113**, 043110 (2013).

[82] M. K. Shakfa, M. Wiemer, P. Ludewig, K. Jandieri, K. Volz, W. Stolz, S. D. Baranovskii, and M. Koch, Thermal quenching of photoluminescence in Ga(AsBi), J. Appl. Phys. **117**, 025709 (2015).

[83] S. Imhof, A. Thränhardt, A. Chernikov, M. Koch, N. S. Köster, S. Chatterjee, S. W. Koch, X. Lu, S. R. Johnson, D. A. Beaton, T. Tiedje, and O. Rubel, Clustering effects in Ga(AsBi), Appl. Phys. Lett. **96**, 131115 (2010).

[84] S. Nargelas, K. Jarašiūnas, K. Bertulis, and V. Pačebutas, Hole diffusivity in GaAsBi alloys measured by a picosecond transient grating technique, Appl. Phys. Lett. **98**, 082115 (2011).

[85] A. Mascarenhas, Yong Zhang, Jason Verley, and M. J. Seong, Overcoming limitations in semiconductor alloy design, Superlattices Microstruct. **29**, 395 (2001).

[86] K. Kim and A. Zunger, Spatial Correlations in GaInAsN Alloys and Their Effects on Band-Gap Enhancement and Electron Localization, Phys. Rev. Lett. **86**, 2609 (2001).

[87] J. W. Matthews and A. E. Blakeslee, Defects in epitaxial multilayers: I. Misfit dislocations, J. Cryst. Growth **27**, 118 (1974).

[88] Paul Voisin, Heterostructures of lattice mismatched semiconductors: Fundamental aspects and device perspectives, Proc. SPIE Int. Soc. Opt. Eng. **0861**, 88 (1988).

Chapter 5

Alloying 2D GaN for optical emitters

Submitted to Physical Review B. Original copy found at https://arxiv.org/pdf/1707.04625v1.pdf. Subject to change.

5.1 Author's Contribution

- All research with the exclusion of unfolding
- Contributions to concept and design of research
- Manuscript writing

Alloying 2D GaN for optical emitters

C. Pashartis and O. Rubel[*]
Department of Materials Science and Engineering, McMaster University,
1280 Main Street West, Hamilton, Ontario L8S 4L8, Canada
(Dated: July 18, 2017)

The recent progress in formation of two-dimensional (2D) GaN by a migration-enhanced encapsulated technique opens up new possibilities for group III-V 2D semiconductors with a band gap within the visible energy spectrum. Using first-principles calculations we explored alloying of 2D-GaN to achieve an optically active material with a tuneable band gap. The effect of isoelectronic III-V substitutional elements on the band gaps, band offsets, and spatial electron localization is studied. In addition to optoelectronic properties, the formability of alloys is evaluated using impurity formation energies. A dilute highly-mismatched solid solution 2D-GaN$_{1-x}$P$_x$ features an efficient band gap reduction in combination with a moderate energy penalty associated with incorporation of phosphorous in 2D-GaN, which is substantially lower than in the case of the bulk GaN. The group-V alloying elements also introduce significant disorder and localization at the valence band edge that facilitates direct band gap optical transitions thus implying the feasibility of using III-V alloys of 2D-GaN in light-emitting devices.

Two-dimensional (2D) materials have demonstrated utility in various technologies such as transistors, photodetectors, and supercapacitors[1–3] enabling new functionalities (flexible, transparent electronics) and further device miniaturization[4,5]. The current portfolio of materials for optoelectronic device applications is dominated by bulk III-V semiconductors. 2D III-V materials feature a wide range of band gaps that span the entire visible spectrum[6–9], which makes them potentially useful in optoelectronics. Drawbacks of 2D III-V monolayers are their much heavier effective masses, when compared to their bulk counterparts, an indirect band gap character, and formability issues[8]. The experimental realization of 2D III-V's beyond hexagonal-BN is extremely challenging due to the high energy difference of $0.3 - 0.6$ eV/atom between the 2D and bulk structures[8].

Al Balushi et al. [9] recently reported the growth of 2D-GaN via a migration-enhanced encapsulated technique with the use of graphene to enclose a bilayer GaN and maintain its structural stability. This pioneering study opens a possibility to overcome a formability issue by manufacturing a few-layer 2D III-V semiconductors. Although the planar monolayer GaN has an indirect band gap of $E_{\mathrm{g}} \approx 4$ eV, a few-layered 2D-GaN is a direct band gap material with a tuneable band gap of $E_{\mathrm{g}} \approx 4 - 5.3$ eV depending on the layer thickness[8,9]. The larger band gap of 2D-GaN *vs* the bulk GaN is attributed to quantum confinement effects. The quantum confinement effects are also responsible for an enhanced exciton binding energy E_{ex}. A binding energy of the order of 1 eV is expected for 2D-GaN due to a linear scaling $E_{\mathrm{ex}} \sim E_{\mathrm{g}}/4$ between the band gap and the exciton binding energy of 2D semiconductors[10]. This result for the exciton binding energy subtracted from the values of the band gap energy implies that blue-ultraviolet emissions are possible with 2D-GaN, whereas transition metal dicalcholgenides exhibit lower optical transition energies of $1-2$ eV[4,5,11] even though the true band gaps are substantially higher because of the strong excitonic effects[12]. The blue-ultraviolet energy spectrum of 2D-GaN raises a question about possibility of alloying the material with other III-V elements to tune the emission wavelength across the visible spectrum.

In this Letter, we probe the effects of isoelectronic substitutions on spatial electron localization, changes in band gap energies, band edge offsets as well as solubility of impurities in the host 2D-GaN utilizing the density functional theory (DFT) package, Vienna *ab-initio* simulation program (VASP)[13,14]. PBEsol[15] was used as the exchange-correlation functional since it accurately captures structural properties and the strength of GaN chemical bonds. The calculated formation enthalpy of $\Delta_{\mathrm{f}}H = -1.29$ eV for wurtzite GaN is in a good agreement with the range of experimental values -1.63 eV[16] and -1.34 eV[17]. Plane-augmented wave potentials[18] were used with *spd* and *sp* valence electrons for group-III and V elements, respectively. The Brillouin zone of the 2D-GaN primitive unit cell was sampled with a $8 \times 8 \times 1$ k-mesh. The full structural optimization was performed with an energy convergence criteria of 10^{-6} eV and the plane-wave cutoff energy of 500 eV. The resultant lattice constant of the 2-atom primitive planar GaN cell corresponded to 3.18 Å after relaxation. Each 2D structure had a fixed vacuum spacing of 20 Å to ensure the monolayer nature of the system.

Impurities were modelled using a supercell technique. We substituted a single group-III/V element into its associative isoelectronic site in a host GaN 128-atom planar 8×8 supercell corresponding to $\approx 1.6\%$ dilution. Supercell calculations were undertaken with the corresponding downscaled k-mesh. Internal relaxation of atomic positions due to impurities was performed using a force convergence of 0.01 eV/Å while maintaining the macroscopic lattice parameters of the host 2D-GaN. Relativistic effects (the spin orbit interaction) were simulated for supercells with In, Tl, Sb, and Bi impurities. The K and Γ-points were examined as they correspond to valence and conduction band edges. Presence of a large vacuum space enables band offset calculations to within 30 meV of an error for heavier elements via a direct comparison of the band edge eigenvalues, i.e., without additional techniques to account for a reference energy shift. Born-effective charge calculations were done using both the self-consistent response to a finite electric field and perturbative[19] approaches due to

---

[*] rubelo@mcmaster.ca

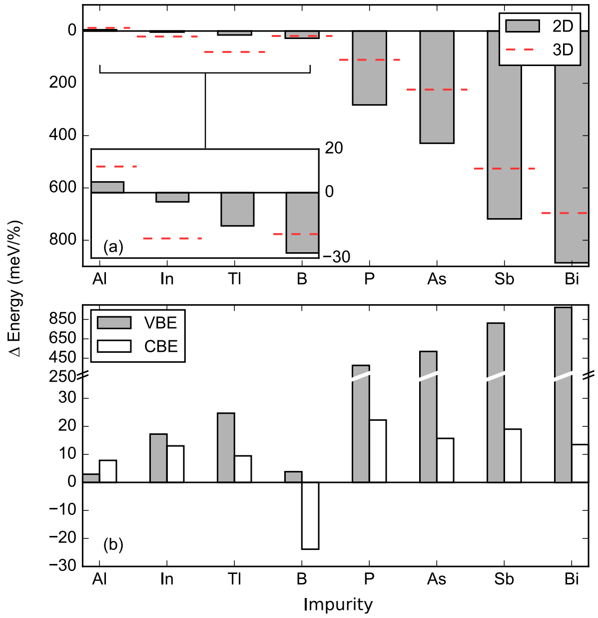

FIG. 1. (a) The band gap change per percent concentration of III-V substitutional isoelectronic elements in 2D-GaN and bulk GaN. (b) Respective shifts of the valence and band edges (VBE and CBE) relative to the host 2D-GaN.

numerical issues. Calculations for the bulk wurtzite GaN were performed using $8 \times 8 \times 4$ k-mesh for the primitive Brillouin zone. Impurities were introduced in a 128-atom supercell of the size $4{\times}4{\times}2$ with a Brillouin zone sampled using a $2{\times}2{\times}2$ k-mesh.

We begin by presenting the results of the band gap changes due to incorporation of individual isoelectronic impurities into the host 2D-GaN structure as shown in Fig. 1a. The group-III elements do not change the band gap significantly with boron reducing the band gap the most in a dilute limit. In contrast, group-V elements affect the band gap much more significantly. Figure 1a includes data for the bulk wurtzite GaN. Notably changes of the band gap due to impurities in the bulk correlate with that in the monolayer. Results for the bulk GaN can be compared to experimental values of the band gap variation taken linearly up to $x = 10\%$ concentration at room temperature: 1 meV/% for $\mathrm{Al}_x\mathrm{Ga}_{1-x}\mathrm{N}$[20,21] and -25 meV/% for $\mathrm{In}_x\mathrm{Ga}_{1-x}\mathrm{N}$[22,23], which are consistent with our results. Furthermore, previous theoretical calculations of wurtzite $\mathrm{GaN}_{1-x}\mathrm{P}_x$ structures yield a band gap variation of -150 meV/% to 10% of P[24], -170 meV/% for 6% of As in $\mathrm{GaN}_{1-x}\mathrm{As}_x$[25], and -400 meV/% for 10% of Sb in $\mathrm{GaN}_{1-x}\mathrm{Sb}_x$[26] that show similar trends to our calculations.

The band offsets due to impurities in 2D-GaN are shown in Fig. 1b. Remarkably all impurities raise the valence band edge (VBE) more than the conduction band edge (CBE) with exception of boron and aluminum. The group-V elements have a much stronger effect on the VBE when substituted in 2D-GaN as compared to group-III elements. Variations in the Born effective charge of impurities shown in Table I aid in explaining this effect. In general, perturbations in the valence band scale with the electropositivity of the substituted element (increase in $Z^* - Z^*_{\mathrm{host}}$). The shift of the valence band edge due to group-V impurities can be viewed as introducing a trap state in the vicinity of the VBE. Similarly, substituting nitrogen into a 2D-GaAs host lattice produces perturbations to the CBE, which correlates with N being more electronegative element than As. This feature is not unique to 2D-GaN and was previously reported for the bulk GaN and GaAs[27–30]. Dilute borides seem to provide the only possibility for engineering a conduction band offset as it is the most electronegative element that can be introduced in the host.

TABLE I. Born effective charges of impurity elements in the host 2D-GaN lattice and localization characteristics at the band edges evaluated using the IPR (χ). The effective charge is highly anisotropic and listed for the parallel ($\parallel$) and perpendicular ($\perp$) directions with respect to the 2D-GaN plane.

Impurity element	$Z^*_{\parallel}$	$Z^*_{\perp}$	χ	
			VBE	CBE
B	2.67	0.45	0.0170	0.0079
Al	2.82	0.45	0.0129	0.0079
In	2.80	0.45	0.0127	0.0078
Tl	2.82	0.45	0.0137	0.0078
P	−1.93	−0.29	0.2614	0.0079
As	−1.74	−0.28	0.4016	0.0079
Sb	−1.38	−0.28	0.2849	0.0080
Bi	−1.18	−0.24	0.4015	0.0080
ref. 2D-GaN	± 3.04	± 0.33	0.0127	0.0078

The lack of a direct band gap in the planar 2D-GaN requires changes in the band dispersion in order to facilitate optical transitions. Localized states due to the impurities relax the momentum conservation requirement and thus enable direct optical transitions. An inverse participation ratio (IPR) criterion that quantifies localization across the structure was introduced by Wegner[31]. It can be viewed as a statistical method that determines a normalized variance of the wavefunction constructed from second moments. Here we use a discrete version of IPR[32] that is evaluated on the basis of probabilities ρ_α of finding an electron with an eigenenergy E_i within the muffin tin spheres centred at atomic sites α

$$\chi(E_i) = \frac{\sum_\alpha^N \rho_\alpha^2(E_i)}{\left[\sum_\alpha^N \rho_\alpha(E_i)\right]^2} . \qquad (1)$$

The summation index α runs over all atomic sites. Here the participation ratio χ^{-1} represents a number of atomic sites, which confine the wave function $\psi_i(\boldsymbol{r})$ with $\chi = 1$ being the upper limit of IPR. The lower limit of IPR, $\chi = 1/N$, is the inverse number of atoms in the lattice that corresponds to extended Bloch states.

The IPRs in our structures at the band edges can be found in Table I. The CBE is insignificantly affected by any of the substitutional elements, even when their incorporation is accompanied by a significant lattice strain due to the size mismatch as in the case of Bi and Tl. The VBE demonstrates a minor increase in localization for group-III elements since Ga and the substitutional elements are electronically similar in the presence of N, as evident from the similar values of the Born

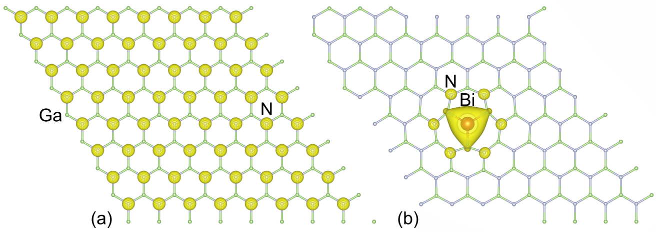

FIG. 2. Isosurfaces of the wave function probability amplitude $|\psi_{n,\mathbf{k}}(\mathbf{r})|^2$ at the valence band edges for (a) $\mathrm{Ga_{64}N_{64}}$, (b) $\mathrm{Ga_{64}N_{63}Bi_1}$ using VESTA[33]. The isosurfaces are plotted at the same values. A large shift in the isosurface is observed to center around Bi. A substution of Al has similar features to the binary structure.

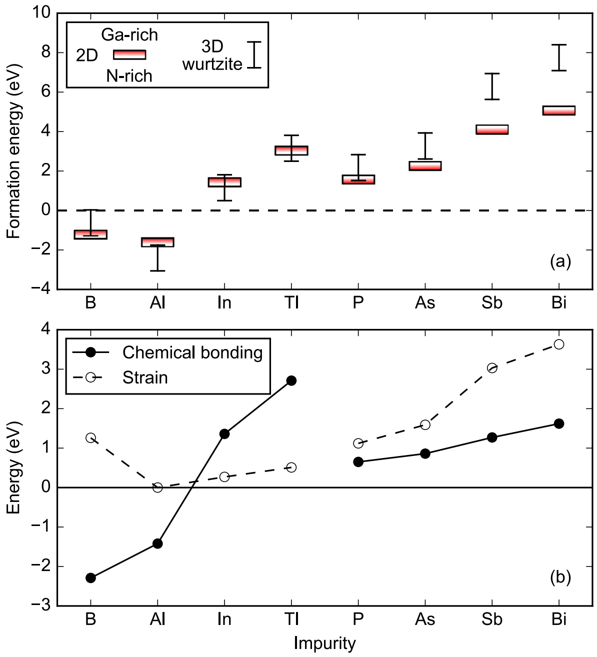

FIG. 3. (a) Formation energies of substituted isoelectronic III-V elements in GaN . The range of values for a given element is associated with Ga or N rich growth conditions. (b) The formation energies are subdivided into the strain energy and change in the chemical energy for 2D-GaN. The chemical trend for group-III elements is governed by the chemical energy, while the strain energy dominates for group-V elements.

effective charges (Table I). The group-V elements introduce strongly localized states in the valence band (an order of magnitude larger IPR), which can be attributed to their much more electropositive nature than N by more than a single elementary charge in $Z^*_{\parallel}$. The localization can be visually observed in Fig. 2. The VBE isosurfaces are centered at the N-sites in the host structure but reside almost entirely on the substituted Bi-atom in GaN:Bi. Chemical trends in localization characteristics of III-V impurities in 2D-GaN are very similar to those previously reported by Bellaiche et al. [28] for the bulk GaN.

The feasibility of incorporating the alloying element into GaN is assessed by calculating defect formation energies due to individual impurity elements following the method outlined in Ref. 34. The defect formation energy (here demonstrated for a general group-III substitution X_{Ga}) is calculated using the DFT total energy of the supercell with an impurity as well as the respective host structure

$$E_{\mathrm{f}}[X_1\mathrm{Ga_{63}N_{64}}] = E_{\mathrm{tot}}[X_1\mathrm{Ga_{63}N_{64}}] - E_{\mathrm{tot}}[\mathrm{Ga_{64}N_{64}}] - \mu[X] + \mu[\mathrm{Ga}]. \tag{2}$$

The DFT total energies of bulk naturally occurring structures are taken to represent the chemical potential of impurities $\mu[X] \approx E_{\mathrm{tot}}[X_{\mathrm{bulk}}]$. The gallium chemical potential is confined within the range

$$E_{\mathrm{tot}}[\mathrm{Ga_{bulk}}] + \Delta_{\mathrm{f}}H[\mathrm{GaN}] < \mu[\mathrm{Ga}] < E_{\mathrm{tot}}[\mathrm{Ga_{bulk}}], \tag{3}$$

where $\Delta_{\mathrm{f}}H$ is the calculated formation enthalpy of GaN (-0.42 and -1.29 eV for the 2D hexagonal planar and bulk wurtzite structures, respectively) determined as

$$\Delta_{\mathrm{f}}H[\mathrm{GaN}] \approx E_{\mathrm{tot}}[\mathrm{GaN}] - \frac{1}{2}E_{\mathrm{tot}}[\mathrm{N_2}] - E_{\mathrm{tot}}[\mathrm{Ga_{bulk}}]. \tag{4}$$

The upper/lower limit of $\mu[\mathrm{Ga}]$ corresponds Ga rich/poor growth conditions.

The results of the defect formation energy calculations are presented in Fig. 3a. Among all III-V elements only B or Al substitutions are energetically favourable. Indium has a limited solubility in the bulk GaN[35], and the same is expected for 2D-GaN due to the similar E_{f} values. The energy penalty associated with the incorporation of a group-V element in 2D-GaN is systematically lower than in the bulk. Due to the relaxed strain conditions in monolayers, 2D materials may generically be more easily alloyed than their bulk counterparts. Phosphorus has a similar defect formation energy to indium in 2D-GaN, which suggest the possibility for practical realization of dilute 2D-$\mathrm{GaN}_{1-x}\mathrm{P}_x$.

To shed light on the physics behind observed chemical trends in the formation energies of the group III-V substitutions, we decomposed the E_{f} values into the strain energy and chemical energy components. The strain and chemical energies are defined as

$$\begin{aligned} E_{\mathrm{strain}} &= E_{\mathrm{tot}}[X_1\mathrm{Ga_{63}N_{64}}] - 63E_{\mathrm{tot}}[\mathrm{GaN}] - E_{\mathrm{tot}}[X\mathrm{N}], && \text{(5a)} \\ \Delta E_{\mathrm{chem}} &= \Delta_{\mathrm{f}}H[X\mathrm{N}] - \Delta_{\mathrm{f}}H[\mathrm{GaN}]. && \text{(5b)} \end{aligned}$$

It can be shown that $E_{\mathrm{strain}} + \Delta E_{\mathrm{chem}}$ correspond to the upper limit of E_{f} in Eq. (2). The values of E_{strain} and ΔE_{chem} attained are presented in Fig. 3b. In the case of boron the high strain energy is compensated by the strong chemical bonding. The incorporation of In and Tl is primarily limited by the weak chemical bonding. In contrast, the solubility of group-V elements is impeded by a high strain energy due to the large variance in the atomic size from the host N.

The analysis of the defect formation energies and the band gap reduction efficiency points to a dilute 2D-$\mathrm{GaN}_{1-x}\mathrm{P}_x$ alloy as a favourable candidate for 2D-GaN-based light emitters in the visible spectrum. With this purpose in mind we investigated optoelectronic properties of $\mathrm{GaN_{0.96}P_{0.04}}$. We have estimated the lattice constant of the $\mathrm{GaN}_{1-x}\mathrm{P}_x$ alloy using Vegard's law. Reduction of the band gap by 0.57 eV is observed with respect to the host 2D-GaN. The effective band

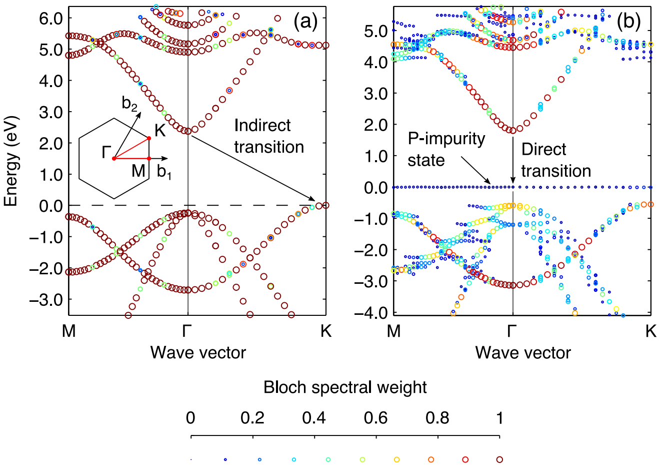

FIG. 4. Effective band structure of a hexagonal monolayer of (a) $Ga_{25}N_{25}$ and (b) $Ga_{25}N_{24}P_1$ supercells. Phosphorus introduces a localized state (without a well-defined Bloch character) above the valence band of the host GaN. A partial Γ-character of this impurity-like state creates a possibility for optical transitions in otherwise indirect band gap 2D-GaN. The origin of the energy scale is set at the Fermi energy.

structure unfolded to a primitive Brillouin zone is shown in Fig. 4. Phosphorous introduces a dispersionless state approximately 0.6 eV above the host valence band. The lack of a well-defined Bloch character is consistent with the strong localization at the VBE for all group-V impurities (Table I).

A non-zero dipole transition matrix element is expected due to a direct optical transition between P-state and the conduction band edge, whose Bloch character at Γ-point is well preserved. Although 2D-$GaN_{0.96}P_{0.04}$ is an optically active material, the dipole matrix element for a direct transition in Fig. 4b is two orders of magnitude weaker than the $\Gamma_c \rightarrow \Gamma_v$ matrix element in the planar 2D-GaN. This result can be attributed to a weak Γ-character of the P-related state as evident from the unfolded band structure. Thus, the intrinsically direct band gap of a few-layered 2D-GaN[9] makes it an attractive alternative to the planar structures for optical emitters. One would expect the behaviour of impurities in a few-layered 2D-GaN to fall between our results for the planar monolayer 2D-GaN and the bulk GaN depending on the layer thickness.

In conclusion, isoelectronic substitutions into a host monolayer 2D-GaN were explored to achieve optical emission with a tuneable wavelength in the visible spectrum. Low-dimensional materials may generally be less strenuous to alloy than bulk materials due to fewer geometrical constraints. Incorporation of phosphorous among other III-V elements enables a much more efficient band gap reduction than indium while featuring similar impurity formation energies. The band gap reduction of the order $-100\ldots-300$ meV per %P in dilute 2D-$GaN_{1-x}P_x$ is mediated by formation of a localized state above the valence band edge of the host 2D-GaN. Concurrently, the conduction band remains resistant to perturbations irrespective of the substitutional element. The phosphorous impurity state facilitates a direct optical transition in otherwise indirect planar monolayer 2D-GaN, which becomes possible due to the electronic localization and the associated relaxation of the wave vector selection rule.

ACKNOWLEDGMENTS

Authors would like to thank Maciej Polak (Wroclaw University of Science and Technology) and Alex Pofelski (McMaster University) for critical reading and valuable discussions. Funding was provided by the Natural Sciences and Engineering Research Council of Canada under the Discovery Grant Program RGPIN-2015-04518. C.P. would like to acknowledge support by the Ontario Graduate Scholarship. This work was performed using computational resources of the Thunder Bay Regional Research Institute, Lakehead University, and Compute Canada (Calcul Quebec).

---

[1] R. Mas-Balleste, C. Gomez-Navarro, J. Gomez-Herrero, and F. Zamora, Nanoscale **3**, 20 (2011).

[2] G. Fiori, F. Bonaccorso, G. Iannaccone, T. Palacios, D. Neumaier, A. Seabaugh, S. K. Banerjee, and L. Colombo, Nat. Nanotechnol. **9**, 768 (2014).

[3] F. H. L. Koppens, T. Mueller, P. Avouris, A. C. Ferrari, M. S. Vitiello, and M. Polini, Nat. Nanotechnol. **9**, 780 (2014).

[4] Q. H. Wang, K. Kalantar-Zadeh, A. Kis, J. N. Coleman, and M. S. Strano, Nat. Nanotechnol. **7**, 699 (2012).

[5] S. Z. Butler, S. M. Hollen, L. Cao, Y. Cui, J. A. Gupta, H. R. Gutiérrez, T. F. Heinz, S. S. Hong, J. Huang, A. F. Ismach, et al., ACS Nano **7**, 2898 (2013).

[6] X. Blase, A. Rubio, S. G. Louie, and M. L. Cohen, Phys. Rev. B **51**, 6868 (1995).

[7] H. Şahin, S. Cahangirov, M. Topsakal, E. Bekaroglu, E. Akturk, R. T. Senger, and S. Ciraci, Phys. Rev. B **80**, 155453 (2009).

[8] H. L. Zhuang, A. K. Singh, and R. G. Hennig, Phys. Rev. B **87**, 165415 (2013).

[9] Z. Y. Al Balushi, K. Wang, R. K. Ghosh, R. A. Vilá, S. M. Eichfeld, J. D. Caldwell, X. Qin, Y.-C. Lin, P. A. DeSario, G. Stone, et al., Nat. Mater. **15** (2016).

[10] Z. Jiang, Z. Liu, Y. Li, and W. Duan, Phys. Rev. Lett. **118**, 266401 (2017).

[11] A. Ramasubramaniam, D. Naveh, and E. Towe, Phys. Rev. B **84**, 205325 (2011).

[12] A. T. Hanbicki, M. Currie, G. Kioseoglou, A. L. Friedman, and B. T. Jonker, Solid State Commun. **203**, 16 (2015).

[13] G. Kresse and J. Furthmüller, Phys. Rev. B **54**, 11169 (1996).

[14] G. Kresse and J. Furthmüller, Comp. Mater. Sci. **6**, 15 (1996).

[15] J. P. Perdew, A. Ruzsinszky, G. I. Csonka, O. A. Vydrov, G. E. Scuseria, L. A. Constantin, X. Zhou, and K. Burke, Phys. Rev. Lett. **100**, 136406 (2008).

[16] M. R. Ranade, F. Tessier, A. Navrotsky, V. J. Leppert, S. H. Risbud, F. J. DiSalvo, and C. M. Balkas, J. Phys. Chem. B **104**, 4060 (2000).

[17] K. T. Jacob and G. Rajitha, J. Cryst. Growth **311**, 3806 (2009).

[18] P. E. Blöchl, Phys. Rev. B **50**, 17953 (1994).

[19] M. Gajdoš, K. Hummer, G. Kresse, J. Furthmüller, and F. Bechst-

edt, Phys. Rev. B **73**, 045112 (2006).

[20] D. Brunner, H. Angerer, E. Bustarret, F. Freudenberg, R. Höpler, R. Dimitrov, O. Ambacher, and M. Stutzmann, J. Appl. Phys. **82**, 5090 (1997).

[21] S. R. Lee, A. F. Wright, M. H. Crawford, G. A. Petersen, J. Han, and R. M. Biefeld, Appl. Phys. Lett. **74**, 3344 (1999).

[22] W. Shan, B. D. Little, J. J. Song, Z. C. Feng, M. Schurman, and R. A. Stall, Appl. Phys. Lett. **69**, 3315 (1996).

[23] T. Matsuoka, H. Okamoto, M. Nakao, H. Harima, and E. Kurimoto, Appl. Phys. Lett. **81**, 1246 (2002).

[24] W. G. Bi and C. W. Tu, Appl. Phys. Lett. **69**, 3710 (1996).

[25] C.-K. Tan and N. Tansu, AIP Adv. **5**, 017129 (2015).

[26] R. M. Sheetz, E. Richter, A. N. Andriotis, S. Lisenkov, C. Pendyala, M. K. Sunkara, and M. Menon, Phys. Rev. B **84**, 075304 (2011).

[27] T. Mattila and A. Zunger, Phys. Rev. B **58**, 1367 (1998).

[28] L. Bellaiche, S. H. Wei, and A. Zunger, Phys. Rev. B **54**, 17568 (1996).

[29] E. P. O'Reilly, A. Lindsay, P. J. Klar, A. Polimeni, and M. Capizzi, Semicond. Sci. Tech. **24**, 033001 (2009).

[30] C. Pashartis and O. Rubel, Phys. Rev. Appl. **7**, 064011 (2017).

[31] F. Wegner, Z. Phys. B: Condens. Matter **36**, 209 (1980).

[32] N. C. Murphy, R. Wortis, and W. A. Atkinson, Phys. Rev. B **83**, 184206 (2011).

[33] K. Momma and F. Izumi, J. Appl. Crystallogr. **44**, 1272 (2011).

[34] C. Freysoldt, B. Grabowski, T. Hickel, J. Neugebauer, G. Kresse, A. Janotti, and C. G. Van de Walle, Rev. Mod. Phys. **86**, 253 (2014).

[35] I. Ho and G. B. Stringfellow, Appl. Phys. Lett. **69**, 2701 (1996).

Chapter 6

Summary

In the first paper, the capabilities of various III-V (InGa)As based alloys for 1.55 μm wavelengths were examined. Isoelectronic substitutions into a host GaAs structure showed the amount of localization introduced at the band edges. Noticeably, the localization introduced was well-correlated with the Born effective charge of the site. It was found that the electropositivity of a substituted element, with respect to the host element, scales with the localization. The greater the difference in Born effective charge from the host site, the more prevalent the changes in localization. These characteristics quantify the changes in carrier mobility and photoluminscence linewidth broadening. Introducing nitrogen into a GaAs host would reduce the band gap but increase the photoluminscence linewidth significantly, an undesirable property. By comparing the localization with existing experimental evidence, it was demonstrated that localization can be useful for the prediction of material properties. Utilizing the host GaAs impurity results and extending the characteristics to (InGa)As, the industry standard material was observed to be disorder-free. Of the other alloy candidates studied, we verified that introducing Bi does increase the spin-orbit split-off. Correspondingly, Bi increases the amount of localization which enhances the inhomogeneous broadening and photoluminscence linewidth of the material.

The second paper explored the alloying capabilities of two-dimensional GaN. Existing two-dimensional materials are not able to span the visible optical spectrum. By alloying two-dimensional GaN, it was shown that a significant reduction in the band gap is achievable with dilute concentrations. A similar method to the telecommunications research was employed to analyze the effects of localization on the band edges. In addition, an evaluation of the defect formation energy was performed. Using a host structure of GaN, isoelectronic substitutions showed no valence band edge localization from the group III elements, but the localization from the group V elements was significant. The cause of the discrepancy was due to the increased Born effective charges of the group V elements, compared to N. An absence of conduction band edge localization for all elements could prove to be useful in devices. It was observed that due to the relaxed strain conditions in two-dimensions, compared to their bulk wurtzite counterparts, alloying is more favourable in a two-dimensional environment. The indirect band gap of GaN is a significant issue for optical emissions, but it was shown that dilute concentrations introduce trap states to favour direct recombination. P was the most promising realistic candidate for decreasing the band gap in dilute concentrations.

Spatial electron localization is an important quantity that can be used to quantify the changes in many optoelectronic properties of a material without time consuming calculations. Chamges in carrier mobility, photoluminscence linewidth, and inhomogeneous broadening can be accounted for using the Inverse Participation Ratio. This numerical technique enables the analysis and tuning of prospective candidates for new semiconductor alloys with desirable parameters.

Bibliography

[1]Z. Y. Al Balushi, K. Wang, R. K. Ghosh, R. A. Vilá, S. M. Eichfeld, J. D. Caldwell, X. Qin, Y.-C. Lin, P. A. DeSario, G. Stone, et al., "Two-dimensional gallium nitride realized via graphene encapsulation", Nat. Mater. **15** (2016).

[2]H. Morkoc, S. Strite, G. Gao, M. Lin, B. Sverdlov, and M. Burns, "Large-band-gap SiC, III-V nitride, and II-VI ZnSe-based semiconductor device technologies", J. Appl. Phys. **76**, 1363–1398 (1994).

[3]J. Geisz and D. Friedman, "III–N–V semiconductors for solar photovoltaic applications", Semicond. Sci. Tech. **17**, 769 (2002).

[4]M. Usman, C. A. Broderick, Z. Batool, K. Hild, T. J. Hosea, S. J. Sweeney, and E. P. O'Reilly, "Impact of alloy disorder on the band structure of compressively strained GaBi_x As_{1-x}", Phys. Rev. B **87**, 115104 (2013).

[5]I. Vurgaftman, J. Meyer, and L. Ram-Mohan, "Band parameters for III–V compound semiconductors and their alloys", J. Appl. Phys. **89**, 5815–5875 (2001).

[6]N. Grote and H. Venghaus, *Fibre optic communication devices*, Vol. 4 (Springer Science & Business Media, 2012).

[7]S. R. Bank, H. Bae, L. L. Goddard, H. B. Yuen, M. A. Wistey, R. Kudrawiec, and J. S. Harris, "Recent progress on 1.55- μm dilute-nitride lasers", IEEE J. Quantum. Elect. **43**, 773–785 (2007).

[8]S. J. Sweeney and S. R. Jin, "Bismide-nitride alloys: promising for efficient light emitting devices in the near- and mid-infrared", J. Appl. Phys. **113**, 043110 (2013).

[9]J. Northrup, C. Chua, Z. Yang, T. Wunderer, M Kneissl, N. Johnson, and T. Kolbe, "Effect of strain and barrier composition on the polarization of light emission from AlGaN/AlN quantum wells", Appl. Phys. Lett. **100**, 021101 (2012).

[10]H. Şahin, S. Cahangirov, M. Topsakal, E Bekaroglu, E Akturk, R. T. Senger, and S. Ciraci, "Monolayer honeycomb structures of group-IV elements and III-V binary compounds: first-principles calculations", Phys. Rev. B **80**, 155453 (2009).

[11]H. L. Zhuang, A. K. Singh, and R. G. Hennig, "Computational discovery of single-layer III-V materials", Phys. Rev. B **87**, 165415 (2013).

[12]R. Mas-Balleste, C. Gomez-Navarro, J. Gomez-Herrero, and F. Zamora, "2D materials: to graphene and beyond", Nanoscale **3**, 20–30 (2011).

[13]G. Fiori, F. Bonaccorso, G. Iannaccone, T. Palacios, D. Neumaier, A. Seabaugh, S. K. Banerjee, and L. Colombo, "Electronics based on two-dimensional materials", Nat. Nanotech. **9**, 768–779 (2014).

[14]F. H. L. Koppens, T. Mueller, P. Avouris, A. C. Ferrari, M. S. Vitiello, and M. Polini, "Photodetectors based on graphene, other two-dimensional materials and hybrid systems", Nat. Nanotechnol. **9**, 780–793 (2014).

[15] F. Xia, D. B. Farmer, Y. Lin, and P. Avouris, "Graphene field-effect transistors with high on/off current ratio and large transport band gap at room temperature", Nano Lett. **10**, 715–718 (2010).

[16] A. Ramasubramaniam, D. Naveh, and E. Towe, "Tunable band gaps in bilayer transition-metal dichalcogenides", Phys. Rev. B **84**, 205325 (2011).

[17] Q. H. Wang, K. Kalantar-Zadeh, A. Kis, J. N. Coleman, and M. S. Strano, "Electronics and optoelectronics of two-dimensional transition metal dichalcogenides", Nat. Nanotechnol. **7**, 699–712 (2012).

[18] S. Z. Butler, S. M. Hollen, L. Cao, Y. Cui, J. A. Gupta, H. R. Gutiérrez, T. F. Heinz, S. S. Hong, J. Huang, A. F. Ismach, et al., "Progress, challenges, and opportunities in two-dimensional materials beyond graphene", ACS Nano **7**, 2898–2926 (2013).

[19] X. Blase, A. Rubio, S. G. Louie, and M. L. Cohen, "Quasiparticle band structure of bulk hexagonal boron nitride and related systems", Phys. Rev. B **51**, 6868–6875 (1995).

[20] Z. Jiang, Z. Liu, Y. Li, and W. Duan, "Scaling universality between band gap and exciton binding energy of two-dimensional semiconductors", Phys.Rev. Lett. **118**, 266401 (2017).

[21] W. Kohn and L. J. Sham, "Self-consistent equations including exchange and correlation effects", Phys. Rev. **140**, A1133 (1965).

[22] F. Giustino, *Materials modelling using density functional theory: properties and predictions* (Oxford University Press, 2014).

[23] D. Sholl and J. A. Steckel, *Density functional theory: a practical introduction* (John Wiley & Sons, 2011).

[24] D. M. Ceperley and B. Alder, "Ground state of the electron gas by a stochastic method", Phys. Rev. Lett. **45**, 566 (1980).

[25] J. P. Perdew and Y. Wang, "Accurate and simple analytic representation of the electron-gas correlation energy", Phys. Rev. B **45**, 13244 (1992).

[26] A. D. Becke, "Density-functional exchange-energy approximation with correct asymptotic behavior", Phys. Rev. A **38**, 3098 (1988).

[27] J. P. Perdew, K. Burke, and M. Ernzerhof, "Generalized gradient approximation made simple", Phys. Rev. Lett. **77**, 3865 (1996).

[28] O. Berolo, J. C. Woolley, and J. Van Vechten, "Effect of disorder on the conduction-band effective mass, valence-band spin-orbit splitting, and the direct band gap in III-V alloys", Phys. Rev. B **8**, 3794 (1973).

[29] H. Deng, J. Li, S. Li, H. Peng, J. Xia, L. Wang, and S. Wei, "Band crossing in isovalent semiconductor alloys with large size mismatch: First-principles calculations of the electronic structure of Bi and N incorporated GaAs", Phys. Rev. B **82**, 193204 (2010).

[30] A. H. Welsh, *Aspects of statistical inference*, Vol. 916 (John Wiley & Sons, 2011).

[31] W. C. Navidi, *Statistics for engineers and scientists*, 3rd ed. (McGraw-Hill New York, 2010), pp. 33–38.

[32] F. Wegner, “Inverse participation ratio in 2+ε dimensions”, Z. Phys. B: Condens. Matter **36**, 209–214 (1980).

[33] C. L. Anderson and C. R. Crowell, “Threshold energies for electron-hole pair production by impact ionization in semiconductors”, Phys. Rev. B **5**, 2267 (1972).

[34] B. Kramer and A. MacKinnon, “Localization: theory and experiment”, Rep. Prog. Phys. **56**, 1469 (1993).

[35] T. Schwartz, G. Bartal, S. Fishman, and M. Segev, “Transport and anderson localization in disordered two-dimensional photonic lattices”, Nature **446**, 52–55 (2007).

[36] O. Rubel, A. Bokhanchuk, S. Ahmed, and E. Assmann, “Unfolding the band structure of disordered solids: from bound states to high-mobility kane fermions”, Phys. Rev. B **90**, 115202 (2014).

[37] A. Zunger, S. Wei, L. Ferreira, and J. E. Bernard, “Special quasirandom structures”, Phys. Rev. Lett. **65**, 353 (1990).

[38] A. van de Walle, P. Tiwary, M. M. de Jong, D. L. Olmsted, M. D. Asta, A. Dick, D. Shin, Y. Wang, L. Chen, and Z. Liu, “Efficient stochastic generation of special quasirandom structures”, Calphad **42**, 13–18 (2013).